

## Deliverable 1.3: Report characterization of SH materials (conductive and non-conductive)

### Self-Healing Soft Robotics

Call identifier: H2020-FET-2019

Grant Agreement: # 828818



<b>Version Number:</b>	V1.0
<b>Authors:</b>	Joost Brancart (VUB) Seppe Terryn (VUB) Guy Van Assche (VUB) Bram Vanderborght (VUB) Tonny Bosman (SUPRA) Jakob Langenbach (ESPCI) Antonia Georgopoulou-Papadonikolaki (EMPA)
<b>Date of preparation:</b>	12/10/2020
<b>Date of last modification:</b>	27/11/2020
<b>Expected delivery date:</b>	30/11/2020

## Executive Summary

Deliverable D1.3 reports on the characterization protocols used to study the developed self-healing materials (SHM) and the comparison of the different studied SHM. First, the main requirements for the SHM in view of the prospected soft robotic applications and demonstrators are reported. These requirements serve as development goals for the functional properties of the SHM. Compromises are sought to achieve the best suited functional performance, while optimizing the self-healing behaviour of the SHM. The report provides **basic protocols** for the synthesis of the different classes of SHM and the characterization of their material properties and self-healing behaviour. These basic protocols describe the minimum characterizations that need to be performed to characterize the SHM and allow straightforward comparison. In addition, **advanced characterization protocols** are proposed to obtain in-depth knowledge of the mechanisms responsible for the reactivity, self-healing behaviour, dynamic mechanical properties and for the electrical conductivity of composites.

The report provides examples of characterization results performed on the different types of SHM from published work and some brief updates of the progress during the project. Non-published data are not discussed given the public nature of this report. Finally, results of the different self-healing materials are compared. Moreover, the different SHM are being validated in the same **soft robotic gripper**. This is the topic of deliverable 2.1, reporting on the prototypes and proofs of concept for self-healing actuators. This will also be the subject of a peer reviewed scientific publication. Electrically conductive composite fibres are being integrated as **sensors** in the same type of soft robotic actuator, such that the self-healing behaviour and mechanical properties of the self-healing materials and the sensor capabilities of the composite materials can be characterized and validated in the same application.

## Table of content

1.	Property requirement for soft robotic applications.....	5
1.1.	Target application and demonstrators .....	5
1.1.1.	<i>Motivation</i> .....	5
1.1.2.	<i>Actuation principles</i> .....	5
1.2.	Mechanical properties .....	6
1.2.1.	<i>Glass transition</i> .....	6
1.2.2.	<i>Elastic behaviour</i> .....	6
1.2.3.	<i>Dynamic behaviour</i> .....	8
1.2.4.	<i>Stress-relaxation and creep behaviour</i> .....	8
1.2.5.	<i>Reprocessability and recyclability</i> .....	8
1.3.	Electrical properties.....	9
1.3.1.	<i>Electrical conductivity</i> .....	9
1.3.2.	<i>Piezoresistivity</i> .....	10
1.4.	Self-healing behaviour .....	10
1.4.1.	<i>Damaging modes and size of damage</i> .....	10
1.4.2.	<i>Healing rate and efficiency</i> .....	11
1.4.3.	<i>Healing repeatability and long-term preservation</i> .....	11
2.	Characterization protocols.....	13
2.1.	Basic chemical characterization.....	13
2.1.1.	<i>Reactants characterization</i> .....	13
2.1.2.	<i>Product characterization</i> .....	14
2.2.	Advanced chemical characterization protocols .....	14
2.2.1.	<i>Reactivity</i> .....	14
2.2.2.	<i>Property development</i> .....	15
2.3.	Basic mechanical characterization protocol .....	16
2.3.1.	<i>Stress-strain behaviour</i> .....	16
2.3.2.	<i>Dynamic mechanical analysis</i> .....	17
2.3.3.	<i>Stress-relaxation</i> .....	17
2.3.4.	<i>Creep behaviour</i> .....	17
2.4.	Advanced mechanical characterization protocols .....	17
2.5.	Electrical properties and mechanoelectrical behaviour .....	18
2.5.1.	<i>The setup for mechano-electrical testing</i> .....	18
2.5.2.	<i>Dynamic Tensile Testing</i> .....	19
2.5.3.	<i>Quasi-Static Testing</i> .....	20

2.6.	Processability .....	20
2.7.	Self-healing assessment.....	21
3.	Results and discussion.....	23
3.1.	Hydrogen-bonded supramolecular networks (SupraPolix).....	23
3.1.1.	<i>Supramolecular materials</i> .....	23
3.1.2.	<i>Functional hybrid supramolecular materials</i> .....	23
3.2.	Diels-Alder-based networks (VUB) .....	23
3.2.1.	<i>Thermally reversible dissociative networks</i> .....	23
3.2.2.	<i>Electrically conductive materials</i> .....	36
3.3.	Double dynamic networks (ESPCI).....	36
3.3.1.	<i>Hybrid vitrimer network</i> .....	36
3.3.2.	<i>Electrically conductive materials</i> .....	47
3.4.	Conductive thermoplastic elastomers (Empa).....	48
4.	References .....	56

## 1. Property requirement for soft robotic applications

### 1.1. Target application and demonstrators

#### 1.1.1. Motivation

The SHERO project is a low technological readiness level (TRL) project in which new self-healing (SH) materials, processing and manufacturing techniques, soft sensors, novel actuators and smart controllers for soft robotics are developed. The target application scenario for demonstrating the capabilities of these fundamental new building blocks will be focused on soft grippers, due to the following motivations:

1. Soft grippers represent a large part of the current and future market of soft robotics. The consortium believes that this application will be the fastest to be widely adopted in the manufacturing, automation and robotics industries. This prediction is emphasized by the first companies, like Softrobotics Inc. [1], Empire Robotics [2], Onrobot [3], Piab [4], Soft Robot Tech [5], and Rechu Softroboticgripper [6] that commercialized different types of soft grippers.
2. Soft grippers [7,8] are used in a wide variety of robotic subfields, including industrial pick and place robots [9,10], food packaging [11,12], agriculture robots for picking fruits and vegetables [13], prosthetics [14], social robots [15] and surgical robots [16,17].
3. Soft grippers are a suitable demonstrator for an integrated autonomous self-healing capacity, because being continuously in contact with external objects they are most likely to get damaged by sharp objects. In addition, they are prone to damage caused by cyclic loading, including fatigue and interfacial debonding (see *A review on self-healing polymers for soft robotics*).
4. Failure in these grippers can lead to expensive maintenance performed by employees or experts and non-negligible offline times.

Soft grippers are currently developed from non-recyclable materials and their limited lifetime will lead to a non-ecological application in the future.

#### 1.1.2. Actuation principles

Most of the soft grippers are actuated through variable length tendons [18], which can be integrated tension cables or shape memory alloy cables [19], or through shape memory polymers [20,21], or they are pneumatically driven by placing their internal fluidic channels and chambers under pressure [22,23] or under vacuum [24]. In the SHERO project we focus on pneumatic actuation and tendon actuation driven by electrical motors, because compared to the other actuation mechanisms, they are superior in:

1. *Force and power output.* Both essential for the soft grippers to handle objects with weights in the 10 g – 1 kg range.
2. *Actuation speed and actuator dynamics.* For soft gripper applications the actuation speed should be in the order of 0.1 – 10 seconds, and preferably as fast as possible.

## 1.2. Mechanical properties

The healing ability will be introduced into soft robots by constructing the flexible structural components out of SH polymers. Although SH glassy thermosets [25] can be used to make healable stiff components for (soft) robotics, the focus of this review is on elastomers. In addition, the segmental mobility in elastomers is orders of magnitude greater in comparison with the mobility in thermoset networks, which allows healing at lower temperatures and even in some cases at room/application temperature. Moreover, elastomers with a limited viscous contribution in their viscoelastic behaviour are preferred, to avoid undesired phenomena like stress-strain hysteresis and creep, which have a negative effect on the energy efficiency and the dynamics of the soft robotic components. Hence, the elastic recovery is preferred to be fast and complete. Preferentially the mechanical strength and moduli are high as this ensures higher force and power output of the robotic systems that are constructed from them. In addition, the elastomers need to be able to be reshapeable through temperature treatment. This allows constructing complex robotic parts and recycling them at the end of life.

### 1.2.1. Glass transition

In polymer networks, the **glass transition** is a reversible and gradual transition of the amorphous phase from a hard brittle state into an elastomeric state. In a fully cured network polymer, a single **glass transition temperature ( $T_g$ )** is usually defined, although the transition can be as much as 100 K wide. Depending on the application temperature ( $T_{\text{application}}$ ) the material will be a thermoset or elastomer.

- $T_g > T_{\text{application}}$ : at application temperature the polymer network is in a thermoset state, the material is hard and glassy. Upon applying stress, the thermoset shows very little strain.
- $T_g < T_{\text{application}}$ : at application temperature the polymer network is an elastomer. The material is flexible and relatively large strains can be created upon applying stress.

In the glassy state, there is very little mobility on the segmental level. Consequently, this state is characterised by a high elastic modulus (GPa) and a small strain upon fracture (a few %). In the elastomeric state, there is extensive segmental mobility at the molecular level, secondary interactions can be reversibly broken and polymer chains can be (partially) disentangled. As a result, the elastomeric network has a much lower elastic modulus (MPa) and high fracture strains (100 - 1000%). As for the soft robotics application, self-healing polymers with an elastomeric behaviour are preferred, the glass transition temperature of the self-healing polymers should be below  $T_{\text{application}}$ . For soft robotic grippers we define the application temperature window between -5 °C and 35 °C. It is preferred that the glass transition temperature is at least 20 K below the application window in order to ensure stable mechanical properties during applications, so the  $T_g$  is preferably below -25 °C.

### 1.2.2. Elastic behaviour

The **Young's modulus** is a measure for the elastic behaviour of an elastomer. For soft (continuum) robotic applications elastomeric materials with Young's moduli between 100 kPa and 0.5 GPa are used in general. To increase the force and power output of the soft robots higher Young's moduli (> 1 MPa) are required. The **hardness** of a material is a measure of the resistance against indentation, and is also commonly used as a measure for the elastic behaviour of elastomeric materials. For elastomeric materials, hardness values can be related to the elastic moduli of the materials. Many different scales are used due to the different types of indentors used to measure the hardness, e.g. Shore hardness commonly used for elastomers.

In soft robots, body parts, or in some cases the entire robot, consist of a continuously deformable structure. The soft body parts have a comparatively large number of degrees of freedom, leading to

interesting large-scale deformation modes. To achieve these deformation modes, the material of which these components are made of, needs to be strained over a broad range. A strain window for soft pneumatic grippers was defined based on finite element method (FEM) modelling in Abaqus (Figure 1) of the actuation of a bending soft pneumatic actuator, the design of which is based on PneuNets designs that are well described in literature [23,26,27]).

For this particular design, strains between  $-20\%$  and  $130\%$  are registered and as such for this application the self-healing material should be able to be strained to at least  $130\%$ . Although the highest strains are measured locally only (Figure 1), the material still must be able to withstand these to avoid damage due to overloading, as it would lead to bursting of the actuator. This maximum strain requirement is highly influenced by the design of the bending actuator (wall thickness, geometry, ...). However, in order to have a higher design freedom for future soft gripper design, these simulations illustrate that in order to achieve relevant deformations the maximum strain for elastomers for soft robotics should be substantially high (e.g., in this case  $> 130\%$ ). The material should also be able to withstand compression strains up to  $-20\%$ . Many more designs were simulated using FEM, but these will be described in (Deliverable 2.1). To achieve interesting deformations the elastomers should at least be able to reach  $100\%$  of strain without the occurrence of fracture.

The typical strains expected for sensors depend on the location where the sensor is integrated into the robotic component. The sensors will not undergo the maximum strains as seen in the FEM simulation of the PneuNet (Figure 1: Finite element modelling in Abaqus of a PneuNet bending actuator design that is pneumatically actuated. Strains up to  $130\%$  are registered in specific locations. ). The sensor morphology and location will be chosen such that the sensor is sensitive to the deformation (motion) of the finger and can be used to track the position of the end vector. Typical strains in this example would range from  $0$  to  $50\%$ .

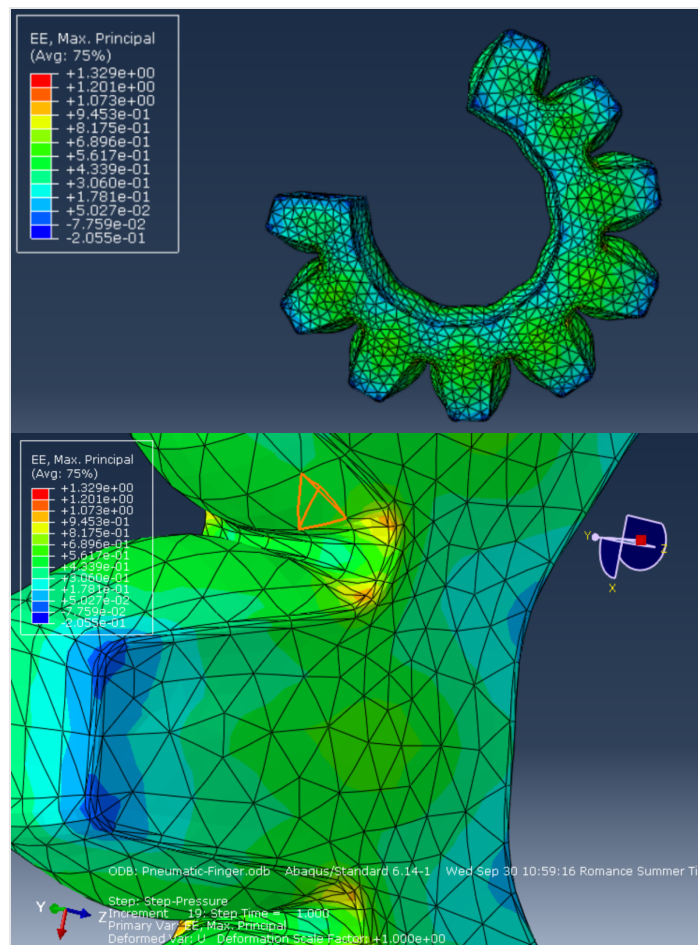


**Figure 1: Finite element modelling in Abaqus of a PneuNet bending actuator design that is pneumatically actuated. Strains up to 130 % are registered in specific locations.**

### *1.2.3. Dynamic behaviour*

Soft robotic components undergo strains of up to 100 % in the order of seconds. Typical strain rates that the elastomeric materials undergo range up to the order of 1000 % min<sup>-1</sup>.

The dynamics of a soft robotic gripper are preferentially as fast as possible and depend on the (visco)elastic response of the elastomer used to construct the actuators. Materials with a predominantly elastic response (and negligible viscous response) will react fast (strain) to applying/releasing stress. Consequently, elastomers with a very low viscous contribution in the viscoelastic response are preferred (ideally <1%). A higher viscous contribution in the viscoelastic response leads to an increased undesired stress-strain hysteresis during loading and unloading cycles of the elastomeric material, as more energy is dissipated in the form of heat. The result is a decrease in energy efficiency of actuation cycle and slower strain recovery, which is detrimental for the actuator dynamics. Elastic recovery is preferentially achieved in less than 10 seconds for strains up to 100%, however, slower recovery might still be adequate depending on the application.

### *1.2.4. Stress-relaxation and creep behaviour*

Both stress-relaxation and creep should be as minimal as possible. Stress-relaxation can lead to decreased power/force output and leads to a time-dependent response of the actuator that complicates the control of the soft gripper. Creep, a permanent plastic deformation of the material due to a continuously applied stress, is unacceptable for soft robotic applications, as it leads to a constant decrease in actuator performance. Consequently, creep should be negligible in the strain window (e.g., 0 – 130 %) of the soft gripper application.

### *1.2.5. Reprocessability and recyclability*

In general, the components in soft robotics are of a medium to high degree of complexity. Therefore, manufacturing techniques like injection moulding, compression moulding, and additive manufacturing are increasingly used (see deliverable D1.5). In these manufacturing processes, solid pellets or filaments are reshaped into (complex) components and, consequently, they require reprocessability of the used polymer. If the self-healing polymer can be reprocessed, processing techniques providing a high design freedom will be available for future manufacturing of SH robotic components. In addition, SH polymers that can be reprocessed/recycled, further contribute to the development of a sustainable technology and eco-friendly soft robotics.

For reshaping and/or recycling of the self-healing polymer networks, the SHM must exhibit a viscous flow behaviour at elevated temperatures. Depending on the processing and manufacturing techniques and the available equipment within the consortium, a range of viscosities can be defined for which the technique can be used in practice:

- (Direct) Injection moulding: 10<sup>2</sup>-10<sup>3</sup> Pa.s (at relevant temperature and shear rate)
- Fused filament fabrication (extrusion): 10<sup>2</sup>-10<sup>6</sup> Pa.s
- Compression moulding: 10<sup>2</sup> Pa.s

The processing temperature at which viscous flow is achieved should be at least 50 °C above the intended application temperature. For soft robotic applications this application temperature window can be taken from -15 to 35 °C. If the temperature at which predominantly viscous behaviour is

obtained is too close to the application temperature, the structural stability (shape, geometry ...) cannot reasonably be maintained due to the dynamically reversible nature of the network crosslinking reaction.

### 1.3. Electrical properties

#### 1.3.1. Electrical conductivity

Elastomers are commonly known as insulators but when they are blended with conductive fillers, the resulting composites can be conductive. The conductivity in the composite is the result of the formation of a conductive network of filler particles. The conductivity for these composites is typically between 1 S/cm and 100 S/cm. The percolation threshold is the minimum amount of conductive filler required for converting an insulating matrix to a conductive one. In order to determine the percolation threshold, the conductivity (or resistivity) is plotted against the filler concentration (Figure 2). The curve is then divided in three regions. The first region, at low concentrations is known as the insulation region and there the filler particles are separated from each other without forming a continuous conductive network. For that range of concentrations, the composite behaves as an insulator. In the next region, known as the transition region, there is a sharp increase in the conductivity and in this region is where the percolation threshold can be found. In this region, the continuous conductive network is formed. In the region for high filler concentrations, known as the conductive region, the filler concentration is larger than the required concentration to form a conductive network. As a result of the excess in filler concentration, aggregates and agglomerates of the conductive filler appear inside the matrix. Depending on the combination of matrix and filler, the presence of agglomerates of the filler in the conductive network could influence the electromechanical properties of the resulting composite.

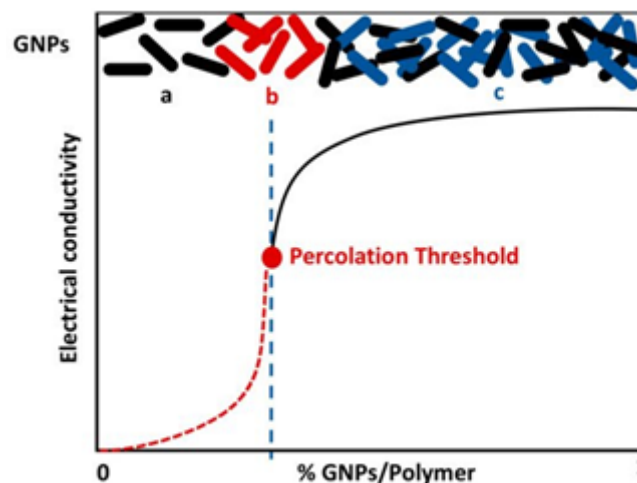


**Figure 2: An example of a percolation curve for a conductive polymer based on a graphene Nanoplatelets filler. Reproduced under the terms of a CC-BY license from: *Polymers* 2020, 12(10), 2189.**

The conduction mechanism, in composites depends on the electron transport through the conductive network, and therefore the percolation threshold depends on factors that influence the electron transport inside the composite. Some important parameters that affect the percolation threshold are the type, dispersion and size of the filler. For example, fillers that have a large aspect ratio, a large surface to volume ratio, facilitate the network formation inside the composite and the electron transport, resulting in a lower percolation threshold than for fillers with smaller aspect ratio. As for the dispersion, the interaction between the filler matrix and also the processing method can influence the

filler dispersion and therefore the conductive network and the percolation threshold. Different options in the processing can be found when the filler is mixed directly in the insulating matrix or by blending a pre-compounded masterbatch with the insulating polymer. The electrical conductivity in conductive composites depends on temperature. This influence is particularly pronounced close to the percolation threshold and is attributed to changes in the conductivity of the polymer. Structural changes in the matrix of the composite caused by the temperature, like swelling effects, also affect the conductive network. This dependency of the conductivity on the temperature is known as the positive temperature coefficient (PTC) effect and it is used for the development of thermistors.

### 1.3.2. Piezoresistivity

Elastomer-based piezoresistive sensors are used in applications that require flexible electronics because of their ability to endure large elongations. Besides their exceptional flexibility, the elastomer based piezoresistive sensors must possess specific characteristics related with their sensor behaviour and more specific with their electro-mechanical response. Piezoresistive elastomer sensors can translate changes in strain to changes in electrical resistance. Therefore, a significant requirement for a piezoresistive elastomer-based strain sensor is the *sensitivity*, which is defined as the ratio between the output signal (resistance) and the measured property, which is in this case is the strain. A good sensor is characterized by a large sensitivity and ideally combined with a *linear response*. For a linear sensor signal, the *gauge factor* is defined as the ratio of relative change in electrical resistance to the mechanical strain. The minimum requirement for a piezoresistive elastomer-based sensor is to have a gauge factor equal or larger than 1, but for a good response the gauge factor should be well above the value of 10. The *noise* should be minimal in the sensor response and, ideally, the sensor should exhibit low sensitivity on stimuli other than strain, like temperature and humidity.

Especially for robotic applications, another important aspect of the sensor response is the *reproducibility* of the sensor signal. Because of viscoelasticity and creep related to the elastomeric matrix of the sensor, there can be *drift* and *uncertainty* observed in the sensor response. For elastomer-based sensors, the uncertainty is linked with a loss of linearity, especially in the unloading of the sensor signal. It is defined by the value of the strain when the loss of linearity appears. Both the drift and the relaxation depend on the maximum strain applied to the sensor signal. In general, in soft robotic applications and wearable electronics, the strains exerted on the sensor should not exceed the value of 50%. For this range of strains, ideally, the *drift* should be below 2%, but values below 5% can be considered acceptable, depending on the required accuracy demanded by the application. As for the uncertainty, values below 2% can be considered negligible for a range of strains of 50% or higher. Another aspect that is particularly important for elastomer-based sensors is the relaxation response of the sensor signal, which is linked with the viscoelasticity of the elastomer matrix. The *relaxation* of the electrical signal is particularly important for applications that involve the sensor detecting the same value of strain over some time. It is desirable that the value of the relaxation should be the minimum amount possible. The value of the relaxation depends on the strain applied and it can be affected by other aspects of the piezoresistive sensor response like the uncertainty and the drift of the sensor signal.

## 1.4. Self-healing behaviour

### 1.4.1. Damaging modes and size of damage

Due to the flexibility of the synthetic materials, soft robots are prone to a number of macroscopic damaging modes:

1. **Damage by sharp objects:** The soft parts are highly susceptible to cuts, tears and perforations caused by sharp objects present in the uncontrolled.

2. **Damage by overloading:** When overloading a soft robotic component, the induced stresses can exceed the mechanical strength of the elastomer, which can lead to rupture of the flexible body of the robot.
3. **Interfacial debonding:** Due to multi-step moulding in the manufacturing of soft grippers or in multi-material soft grippers, weak (multi) material interfaces are created that rely mostly on secondary (physical) interactions. Upon extensive loading or multiple actuation cycles, these weak interfaces fail and interfacial debonding occurs. Researchers often refer to this phenomenon as delamination.
4. **Fatigue:** As typically a large part of the soft robot's body undergoes cyclic deformation upon operation, these parts are susceptible to fatigue, the formation of microdamages due to cyclic loading, which gradually propagate into larger macroscopic damages and eventually failure of the components.

As all these damaging modes result in macroscopic damage that leads to partial or complete failure of the soft robotics gripper, the focus in the SHERO project will be on the detection and the healing of macroscopic damages in self-healing elastomers that lead to noticeable changes in the performance of the actuator. Smaller damages are assumed to heal faster and more effectively. Although surface contamination of the damaged parts by dust and dirt particles can influence the healing process, at this low TRL level the self-healing tests are performed in a clean lab environment.

#### 1.4.2. Healing rate and efficiency

The healing is preferably as fast as possible as offline times of the soft gripper, or soft robots in general, lead to economic losses and should always be minimized. The economical trade-off between the costs resulting from offline time during healing and maintenance cost for repair or replacement highly depends on the future application. The *effectiveness of the healing and the time to reactivation* will depend on the size and location of the damage. As described in our publication in IEEE-RAM [28], depending on the size and location of the damage, the material properties must be completely recovered locally, or in other cases only partially, in order to regain normal operation or operation with a temporarily slightly decreased performance. This can only be tested and described at the actuator level in Deliverable 2.1.

The control of soft robotic components depends on accurate knowledge of the structure and mechanical properties of the components. In order to maintain full performance and to retain control capabilities, the material properties should be completely preserved/recovered within the adequate deformation/actuation range of the component [28]. As a result, the *healing efficiency*, which is based on the recovery of material properties, including the mechanical properties, healing properties, and others, such as electrical conductivity, should be 100% in the useful range for the intended application. Ideally, the material properties are fully recovered over the widest range of stress and strain behaviour. Although not preferred, to some extent, an incomplete recovering could be compensated by a recalibration for control and sensor purposes.

#### 1.4.3. Healing repeatability and long-term preservation

Soft robots will meet various dangerous situations while exposed to an unstructured and dynamic environment and can be damaged multiple times. Similar to the human body, specific locations will be more likely to be exposed to damage events, e.g., the contact surfaces of soft grippers, external surfaces, surfaces touching tendons, or locations having higher stress concentrations during actuation. Consequently, damage is likely to occur multiple times in such locations. The healing mechanism should therefore allow multiple damage-healing cycles at a single location.

**Table 1 Basic property requirements and basic characterization protocols**

Basic property requirements	Technique	Basic characterization protocol
Reactant structure	FTIR-spectroscopy NMR-spectroscopy	ATR or transmission, min 16 scans, 4 cm <sup>-1</sup> <sup>1</sup> H: 5-25 mg, <sup>13</sup> C: 50-100 mg, in deuterated solvent
Reactant physical properties	Thermal analysis	Heat-cool-heat at 10 K.min <sup>-1</sup> below degradation
Product purity	Spectroscopy	See above
Product physical properties	Thermal analysis	Heat-cool-heat at 10 K.min <sup>-1</sup> below degradation
Mechanical properties (Young's modulus, hysteresis, fracture stress and strain)	Mechanical testing	1, 10 and 100 % min <sup>-1</sup> loading/unloading, until failure at 25 °C
Creep behaviour	Mechanical testing	Fixed load of 10% of $\sigma_{max}$ for certain time at 25 °C
Electrical properties	Conductivity test Electromechanical testing	2-point resistance measurements See section 2.5
Self-healing behaviour	Mechanical testing	See section 2.7

**Table 2 Advanced property requirements and advanced characterization protocols**

Advanced property requirements	Technique	Advanced characterization protocol
Chemical reaction kinetics	Spectroscopy Calorimetry	Time-resolved analysis at controlled temperature Experiments at different heating rates and isothermal conditions Modelling of reaction mechanism and kinetics
Property development	Rheometry Mechanical testing	Multi-frequency experiments with dedicated T-program See section 2.3 Modelling of property build-up
Mechanical properties	Mechanical testing	Experiments with complex loading and straining cycles, w/o intermediate healing
Dynamic mechanical behaviour	Dynamic mechanical analysis	Heating 1 K.min <sup>-1</sup> , 0.2% strain, 1 Hz, tension Stepwise isothermal frequency sweeps (TTS)
Stress relaxation behaviour	Mechanical testing Rheometry	See section 2.3.3 Stress relaxation in shear mode (15 mm parallel plates), applying strains 1%-50% until full relaxation
Creep behaviour (cyclic)	Mechanical testing or DMA	Cyclic creep experiments are performed at with alternating loading of the samples for a fixed time (typically 1 h)

## 2. Characterization protocols

Characterization protocols are required on different levels of the material development:

- First, protocols are required for the quality assessment of the starting reactants by determining their chemical structure, purity and related physical and chemical properties, prior to synthesis.
- Second, the synthesized products (oligomers, polymers and networks) need to be characterized to determine the extent of reaction, functionalization, network formation,... Moreover, their functional properties (mechanical, electrical ...) need to be characterized in view of the intended applications. The processability and ease of manufacturing of the SHM is an important criterion that needs to be considered for the characterization of the final products and, in addition, reprocessability and recycling are appreciated properties that are further considered.
- Finally, protocols for the assessment of the self-healing behaviour of the SHM are detailed.

A **basic characterization protocol** is set up to include (i) the mandatory chemical investigations of the starting reactants and final products and (ii) the basic mechanical (actuator material) and electrical (sensor material) property assessments that serve as an eligibility check based on the basic requirements detailed in the previous section of the report. The different steps of the basic characterization protocol are summarized in Table 1 and summarized in following sections.

More **advanced characterization protocols** are described to complement the basic characterization protocol for materials that meet the basic requirements. Protocols are described for advanced chemical characterization to study the dynamic reactivity and property development of the SHM, more detailed mechanical characterization protocols for actuator modelling, simulations and control purposes and more elaborate electromechanical testing of sensors for sensing, structural health monitoring and feedback. The different options for more advanced characterization are summarized in Table 2 and the different protocols are described in more detail in the following sections. Advanced characterization may also be performed on materials that do not meet the requirements to understand the origin of their failure to meet the basic criteria. Moreover, characterization of state-of-the-art actuator and sensor materials is performed to spur the development of self-healing alternatives.

### 2.1. Basic chemical characterization

To control the final product after synthesis, it is important to perform a minimum characterization of the reactants used to synthesize the product and to fully characterize the obtained product. The basic chemical characterization protocol includes the chemical and thermophysical characterization of both reactants and products. From this information the yield of the synthesis is determined and posttreatment steps or changes to the synthesis procedure may be identified.

#### 2.1.1. Reactants characterization

Prior to the synthesis of new materials, the purity and chemical structure of the reagents need to be confirmed using spectroscopic techniques:

- **Fourier-transformed Infrared (FT-IR) spectroscopy:**
  - ATR or transmission (2 mg in 200 mg KBr), 16 scans, 4 cm<sup>-1</sup>
- **Nuclear magnetic resonance (NMR) spectroscopy**
  - <sup>1</sup>H: 5-25 mg, <sup>13</sup>C: 50-100 mg, in deuterated solvent

The (thermo)physical properties and thermal stability are determined using thermal analysis techniques (recommended heating and cooling rates for a first analysis):

- **Thermogravimetric analysis (TGA)** provides information about the thermal stability of the reactants under predefined atmospheric (inert or oxidative) and thermal conditions.
  - Sample size about 1 mg
  - Heating ramp up to 600 °C at 20 °C min<sup>-1</sup> under nitrogen purge flow (25 ml min<sup>-1</sup>)
  - Heating ramp up to 600 °C at 20 °C min<sup>-1</sup> under air purge flow (25 ml min<sup>-1</sup>)
- **Differential scanning calorimetry (DSC)** is used to determine the thermal transitions of the reactants, such as the glass transition temperature  $T_g$  and/or melting temperature  $T_m$ , as applicable. Furthermore, DSC experiments provide information about the reactivity of the reactants (oxidation, dimerization, side reactions) and the reactive mixtures.
  - Sample size 5-10 mg, 25  $\mu$ L aluminium crucibles, hermetically sealed if evaporation might occur.
  - Heat-cool-heat experiment at 10 °C min<sup>-1</sup> until  $T_{max} = T_{degradation} - 50$  °C.
  - Glass transition temperatures  $T_g$  are calculated at half height of the extrapolated tangents from the glassy and mobile state.
  - Reaction peaks are integrated with linear baselines. Extrapolated onset temperature  $T_{eo}$ , peak temperature  $T_p$  and reaction enthalpy  $\Delta_r H$  are calculated. Analogously for melting and crystallization peaks.
  - The reaction conversion  $x$  at a certain time  $t$  is defined as the ratio of the partial reaction enthalpy released up to that point in time  $\Delta_r H_p$ , divided by the reaction enthalpy for complete reaction  $\Delta_r H_{tot}$ , the latter typically evaluated in a non-isothermal experiment to overcome effects of vitrification [29][30][31][32].

### 2.1.2. Product characterization

The synthesized products need to be characterized following the same protocol as for the reactants. Spectroscopic techniques (FT-IR and NMR) are used to determine changes in the chemical structure of the formed product(s), to calculate the yield of the synthesis reaction and to determine the purity of the product(s). Based on the results of the characterization of the product(s), additional steps may need to be taken to increase the yield of the reaction or to purify the product(s).

Thermal analysis techniques (TGA and DSC) provide additional information about the thermal stability and thermal transitions of the product(s) and about their composition and possible compositional changes. DSC may be used to identify residual reactivity after incomplete reaction.

## 2.2. Advanced chemical characterization protocols

### 2.2.1. Reactivity

Spectroscopic and thermal analysis techniques can be combined to study the reactivity of combinations of reactive functional groups during synthesis (polymer network formation) or after synthesis (dynamic reversible behaviour). The Physical Chemistry and Polymer Science (FYSC) research group is specialized in the study of reaction kinetics and thermodynamics. This was recently demonstrated for the thermoreversible Diels-Alder cycloaddition reaction between furan and maleimide functional groups [33] and for the thermal dissociation of anthracene photodimers [34]. The protocol for such a study is detailed below and will produce the most reliable results if structural information from spectroscopy is combined with thermal and physicochemical information from calorimetry.

- Preparation of the reactive mixture:
  - Weighing the components of the reactive mixture
  - Recording the temperature and time between the start of the mixing of the reactive components and the start of the experiment.
- Non-isothermal heat-cool-heat DSC experiments at
  - different heating rates, e.g., 1, 2, 5, 10, 20 K.min<sup>-1</sup> until  $T_{\max} = T_{\text{degradation}} - 50$  K. The more suitable heating rates will depend on the reactivity of the reactive groups in the temperature range of interest.
- Isothermal DSC experiments
  - at different relevant temperatures, based on the extrapolated onset temperature of the reaction exotherm measured in a non-isothermal DSC experiment at 10 K.min<sup>-1</sup>.
  - during different isothermal times. Ideally, the reaction is studied isothermally until completion at that temperature. The reaction enthalpy is calculated using a horizontal baseline, extrapolated from the end of the isothermal experiment, which should be about 50% longer than the than the estimated width at 10% of the peak height.
  - The isothermal segment is followed by a cooling and heating ramp to measure the  $T_g$  and to identify and determine potential residual reaction in case the reaction did not proceed to completion in the isothermal segment.
- Time-resolved temperature-controlled spectroscopy
  - at different relevant temperatures, based on the heat of reaction measured during the non-isothermal DSC experiment.
  - Spectra are recorded at relevant time intervals, depending on the temperature.

To account for the effect of vitrification at temperatures around and below the glass transition temperature  $T_g$  of a densely crosslinked network system [35] or the effect of crystallization the reactive system [34], the use of calorimetric techniques (often in addition to spectroscopic techniques) is necessary to investigate and understand the full extent of the thermophysical and chemical changes. Modulated temperature DSC experiments (modulation amplitude 0.2 K, period 40 s) are especially useful to study vitrification in isothermal or non-isothermal conditions [36–38].

### 2.2.2. Property development

Using the knowledge of the chemical reaction kinetics and thermodynamics, it is possible to link the chemical structure development to the property development. The viscoelastic properties (storage and loss moduli, phase angle and complex viscosity) of the polymer networks can be recorded as a function of time and temperature using oscillatory measurements in **dynamic rheometry** and, if the material is always solid, **dynamic mechanical analysis (DMA)** under programmed reaction conditions.

- Isothermal network formation starting from the monomer mixture in dynamic rheometry  
Isothermal multifrequency oscillatory time sweep with an amplitude of 0.1-5% and frequencies of 0.1-10 Hz at different temperatures.  
**Gelation** is observed as a decrease in the loss angle from 90° (viscous) to 0° (elastic), and the **gel point** is defined as the point at which the loss angle curves at different frequencies intersect (Chambon and Winter criterium [39])
- Viscoelastic properties as a function of temperature  
Multi-frequency oscillatory temperature ramp with an amplitude of 0.1-5% and frequencies of 0.1-10 Hz.
  - From temperatures well below the glass transition until the rubbery plateau in DMA (in heating, typically at 2.5 K min<sup>-1</sup> and 1 Hz).

- If degelation of the polymer network is expected, the temperature range can be extended by dynamic rheometry.
- For time-temperature superposition (TTS) experiments, step-wise isothermal measurements from  $T_g - 50$  K to  $T_g + 50$  K over a frequency range of 0.03 - 60 Hz, with long enough dwell times to reach stable values.
- Viscosity (rheometry)
  - Shear rate ramp or sweep from  $10^{-4}$  to  $100$  s<sup>-1</sup> at selected temperatures
  - For Newtonian behaviour the viscosity can be determined as the slope of the shear stress as a function of the shear rate. The natural logarithm of the viscosity can be plotted with respect to the reciprocal temperature. More advanced models are required if the molecular structure of the material changes. For the most accurate measurement, cone and plate setups are recommended.
- Notes on sample dimensions and instrument compliance:
  - If available, an instrument compliance calibration should be performed.
  - In dynamic rheometry, solidifying materials are typically studied using aluminium parallel plates with a diameter of about 15 mm for a sample thickness of about 0.5 mm. For stiff elastomers and thermosets the plate size, gap, and oscillation amplitudes may need to be adjusted to match the compliance of the instrument setup according to the manufacturer's recommendations.
  - In DMA, measurements on elastomers are typically performed in tension, on samples of about 15 mm x 3 mm x 0.5 mm. For reproducible clamping, a torque wrench or key should be used and excessive deformation at the clamp should be avoided, however, clamping should be tight enough to avoid slip. For stiff elastomers and thermosets the sample cross section and length, and the oscillation amplitudes may need to be adjusted to match the compliance of the instrument setup according to the manufacturer's recommendations.

If the reaction mechanism and the reaction kinetics are well-known, the structure build-up can be simulated under these conditions and related to the property build-up. Detailed modelling and knowledge of the structure-property relations can be exploited during processing and manufacturing and during the application of the studied materials. This has recently been demonstrated by Roels *et al.* [40] for the additive manufacturing of thermoreversible polymer networks to create self-healing soft robotic systems, using knowledge from earlier research by the FYSC research group [33].

## 2.3. Basic mechanical characterization protocol

### 2.3.1. Stress-strain behaviour

The stress-strain behaviour is studied by recording the force/stress resulting from the application of a displacement/strain increasing at a controlled rate. Stress-strain measurements may be performed in universal tensile testing machines under displacement control or using dynamic mechanical analysis (DMA) instruments under strain rate control. Stress-strain relations are commonly tested in tension:

- Strain rates of different orders of magnitude ranging from 1 to 1000 % min<sup>-1</sup>
  - Until failure
  - Cyclic measurements until relevant maximum strains, e.g., 50 %
- The Young's modulus can be derived from the stress-strain experiments as the tangent to the curve at the limiting strain of 0 % or as the slope in the linear elastic regime.
- The stress-strain curves are generally represented in **engineering stress and engineering strain**, calculated as the force per initial cross-sectional area ( $F/A_0$ ) and the elongation over the initial length ( $L/L_0$ ), respectively. For the analysis of strain hardening effects in elastomers

(deformations well above 10%), or their absence, the **true stress – true strain** curves may be calculated as follows from the engineering values, assuming a uniform deformation (no necking) and constant volume:

$$\begin{aligned}\varepsilon_{true} &= \ln\left(\frac{L}{L_0}\right) = \ln(\varepsilon_{eng} + 1) \\ \sigma_{true} &= \sigma_{eng}(\varepsilon_{eng} + 1)\end{aligned}$$

One must always clarify whether the engineering or true values are used in graphs. All stress and strain values and curves discussed in this document are engineering stresses and strains.

### 2.3.2. Dynamic mechanical analysis

The viscoelastic properties of the SHM can be studied by recording the stress/strain response as a consequence of the application of a sinusoidal strain/ stress input signal, with a predetermined amplitude and frequency. This allows the determination of the storage (energy storage) and loss (energy dissipation) moduli, as well as the loss angle.

- Frequency sweep: 0.01-100 Hz
- Amplitude sweep: 0.01% up to a quarter of the value at failure for similar deformation rates

### 2.3.3. Stress-relaxation

**Stress-relaxation** experiments are typically performed at constant strains of about 1 to 10 %. For the screening of candidate materials for soft robotic applications, the materials should be studied under similar conditions relevant for the application, regardless of the potential difference in material properties.

- Stress-relaxation experiment at a constant strain of 1% until at least 63.2% (=  $e^{-1}$ ) of the stress has been relaxed, at elevated temperatures. A first estimation of the time constant for the stress-relaxation phenomenon can be derived as the time at 63.2% stress relaxation.
- The natural logarithm of the time constants can be plotted with respect to the reciprocal temperatures to derive the Arrhenius parameters for the stress-relaxation behaviour.
- These parameters can then be used to calculate the stress-relaxation time constant at the relevant application temperature, e.g., 25 °C, for comparison.
- Comparison to non-reversible (non-self-healing) polymer network standards (e.g., PDMS).

### 2.3.4. Creep behaviour

**Creep** experiments are performed at constant loads. The loads are chosen such that a relevant deformation is achieved in the material to be able to compare different material compositions and types in a quantitative manner. For the basic creep characterization protocol, only static loads are considered within the linear viscoelastic region (LVR), as this is the common standard for creep evaluation. Section 2.4 discusses advanced creep evaluation protocols.

- Creep experiment at a constant load corresponding to 1% strain, at elevated temperatures.
- Creep experiments can be complemented with creep relaxation experiments, to assess the elastic recovery and plastic contribution of the material after loading.
- Comparison to non-reversible (non-self-healing) polymer network standards (e.g., PDMS).

## 2.4. Advanced mechanical characterization protocols

The stress-strain relation can be obtained for different **deformation modes** by fitting the stress-strain results with a hyperelastic model. Uniaxial tension and compression and bending modes are generally accessible on universal mechanical testing machines and DMA instruments, and can be complemented

by torsion experiments on a rheometer. In addition, biaxial testing (tension and compression) may be performed to achieve the widest range of results, to strengthen the hyperelastic model used to simulate the mechanical behaviour of the materials using FEM for the design and evaluation of soft actuators (Figure 1)

**Stress relaxation** and **creep experiments** can be performed under different deformation modes (shear, tension, torsion, compression). In view of the development of materials for a certain application, the mode chosen should reflect the deformation modes of the application. To understand the underlying phenomena to the greatest extent possible, different deformation modes and different deformation magnitudes (stress relaxation) and loads (creep) should be used to complement the basic protocols proposed in sections 2.3.3 and 2.3.4. The stress relaxation and creep behaviour can then be modelled using Maxwell and Kelvin-Voight models, respectively, to obtain a deeper understanding of the behaviour and more accurate simulations of stress relaxation and creep during realistic actuation conditions. In addition to the typical static tests, cyclic and dynamic tests may be designed to more closely reflect the actuation process of the robotic component. Simulated FEM results using the models based on the static tests can be validated and strengthened using dynamic tests.

## 2.5. Electrical properties and mechano-electrical behaviour

In 2020, Georgopoulou *et al.* have published a review article about elastomer-based piezoresistive sensor materials. It can be summarized, that until now no golden standard is used to characterize the material [41]. Therefore, it is not possible to compare the results between different publications, even if the same material is used. This section will show a possible procedure to investigate fracture properties, dynamic and quasi-static behaviour of elastomer-based sensor materials.

### 2.5.1. The setup for mechano-electrical testing

With the purpose of characterizing the piezoresistive response and the performance of the elastomer-based sensor composite material, tensile testing with the simultaneous measuring of the electrical resistance is performed (Figure 3). A standard tensile testing machine can be used, e.g., a Zwick Roell Z005 (ZwickRoell, Ulm, Germany). Ensuring an appropriate fixation is applied to minimize slipping during the straining can be a challenging point, especially for elastomers, but it can be quite an important aspect for ensuring that the accurate values for the strain are recorded during the testing. A way to resolve the issue is to use pneumatic clamping that applies pressure that can hold the samples stable during the testing.

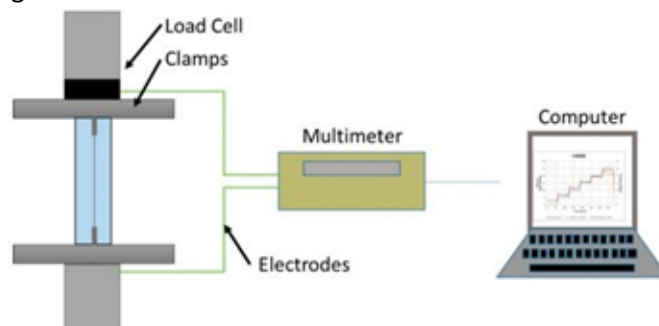


**Figure 3: Tensile test setup for the mechano-electrical characterization of piezoresistive strain sensors with pneumatic grips and multimeter probes. Reproduced under the terms of a CC-BY licence from [42].**

For measuring the electrical signal, a multimeter should be used. In this report, a source meter Keithley 2450 (Keithley Instruments, Solon, USA) was used in combination with the KickStart software from the

same company. A two-terminal sensing mode was used to measure the electrical resistance by measuring the current, while the voltage was held constant at 1 V.

#### *Tensile test up to the point of fracture*

In order to assess the sensitivity and functional range of the piezoresistive strain sensor, a tensile test up to the point of fracture has to be performed. During this test, the samples are strained with a constant rate up to the point of fracture and at the same time, the electrical signal is recorded. The response of the sensor signal during the tensile test up to the point of fracture is a useful indication for the sensitivity of the sensor signal. For that purpose, the relative resistance is plotted against the strain. The **relative resistance** is defined as:

$$R_{rel} = \frac{R - R_0}{R_0}$$

where  $R$  is the measured resistance and  $R_0$  the value of the resistance measured after the sensor was fixed in the tensile machine, e.g., without any straining being applied on the sensor.

A very useful indicator for the behaviour of piezoresistive strain sensor is the slope of the curve relative resistance-strain. If the slope is positive, the response is known as positive piezoresistive response and if it is negative, it is called negative piezoresistive response. Both responses indicate changes in the conductive network caused by the straining. In the case of elastomer piezoresistive strain sensors, both the negative and positive slope can be often seen in different ranges of strain. The slope of the curve is also known as the **Gauge Factor**:

$$Gauge\ Factor = \frac{R_{rel}}{\varepsilon}$$

where  $\varepsilon$  is the value of the strain. Even though the Gauge Factor can be a good indicator for the performance of a piezoresistive sensor, it is only effective for sensors with a linear response over their entire functional range. Otherwise, the range of strain where the Gauge Factor was calculated should always be mentioned alongside the Gauge Factor. An alternative would be to use the product of the Gauge Factor and the strain range as a performance indication.

#### **2.5.2. Dynamic Tensile Testing**

Dynamic testing is performed by exerting cyclic loading and releasing on the sensor. It is a particularly important test for sensors that are used in applications where dynamic conditions are applied, like in soft robotics. This is a test procedure that is often reported in literature [41]. In the case of the dynamic tensile test, it is useful for the characterization to plot the variation of stress and the relative resistance with the time. Especially, for elastomer-based strain sensors, looking at the response of the sensor signal is important for detecting the buckling of the elastomer. Buckling is described as the phenomenon when during the releasing part of a deformation-controlled cycle, the sample does not return to its original length quickly enough. The phenomenon is related to the viscoelastic nature of the elastomer and is linked with the creep effect of the elastomer. This is often observed at low strains and can be detected in the stress-time plot as the strain where the stress becomes zero or negative.

As for the electrical signal during the dynamic testing, an important factor for the repeatability of the sensor response, is the drift for the electrical signal. The **drift** is defined as the percentage difference of the electrical resistance, at the same level of strain, between two different cycles (Figure 4a).

The ideal behaviour for a piezoresistive strain sensor during straining is that the sensor responds in a linear way to the applied strain. However, because of the viscoelasticity of the elastomer matrix, deviation from linear response is often observed. This behaviour is usually observed at low strains and is often expressed as one or more secondary peaks, a change in the slope of the curve, or a lagging phase in the beginning of the loading. The range of strains where the deviation from linearity is observed is known as the **uncertainty** of the sensor signal. The strain where the uncertainty is observed is often recorded to indicate that below this value, the sensor signal cannot be trusted. The dynamic

testing can be performed at different ranges of strains to show how the sensor would respond at the different strains.

**Electrical hysteresis**, another parameter derived by dynamic tensile testing, is defined as the percentage difference of the value of the relative resistance at the same value of strain during the loading and releasing part of the same cycle.

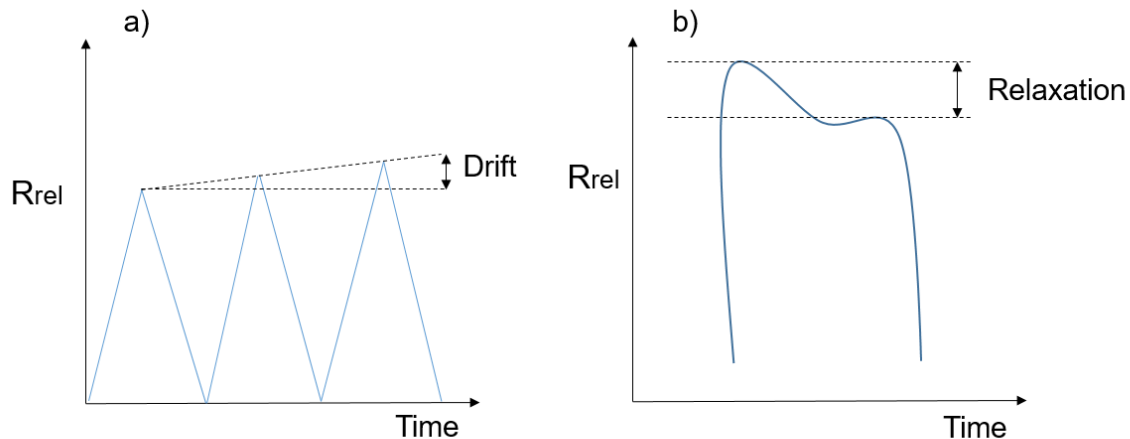


**Figure 4: Definition of the drift and the relaxation for the electrical signal.**

### 2.5.3. Quasi-Static Testing

The quasi-static test involves repeated cycles of loading and releasing with a dwell time at a specific strain. A common practice is to introduce the dwell time at the strain of loading and releasing. The purpose of a quasi-static test is to define the relaxation behaviour of the stress and the electrical signal. Similar to the dynamic tensile testing, the stress and relative resistance is plotted against the time of the test. The **relaxation for the electrical signal** is defined as the percentage difference of the value of the relative resistance at the beginning and end of the dwell time (Figure 4b). The **stress relaxation** is defined as the percentage difference of the value of the stress at the beginning and end of the dwell time.

## 2.6. Processability

The industrial and laboratory standard practice to study the processability of materials and to evaluate certain processing techniques for certain materials is trial-and-error-based. Materials are processed using the processing techniques of interest and chosen processing conditions. The results are then compared to (i) the results from other processing techniques, (ii) using other processing conditions, or (iii) materials that are commonly processed using the evaluated processing technique.

Knowledge of the viscoelastic properties of common standard materials for the processing technique of interest and knowledge of the structure-property relations of the studied materials, or at least knowledge of the viscoelastic properties under the processing conditions, allows to estimate the feasibility of processing under these conditions and to optimize the processing conditions and/or the material behaviour under these conditions. The results of the characterization of the viscoelastic properties from section 2.2.2 can be used to understand the processability.

## 2.7. Self-healing assessment

The protocol for the self-healing assessment in this report limits to the study of the material properties. The self-healing of the different SHM is being validated in the same **soft robotic gripper**. This is the topic of deliverable 2.1. It can already be mentioned that the material does not need to recover all of its mechanical properties completely for the actuator to recover its functional performance, depending on the location and size of the damage and the mechanical limits required for the performance of the actuator [28]. The characterization protocol described below is intended to assess the ability of self-healing materials to recover their functional properties (mechanical, electrical ...), and the rate and efficiency of this recovery.

- Characterization of the healing efficiency of functional property  $X$  (mechanical, electrical ...), having a value for the pristine material prior to damage equal to  $X_0$ .
- Application of damage
  - Controlled damage, applied manually by cutting or puncturing, or applied by loading the sample to a certain percentage of the maximum fracture stress/strain
  - Fatigue loading - applying loading cycles to a selected fraction of the strain at break
  - Testing the material until complete failure
- Characterization of the functional properties of the damaged material  $X_{\text{dam}}$
- Application of the healing procedure (material dependent)
- Characterization of the functional properties of the healed material  $X_{\text{heal}}$

The healing efficiency of the self-healing material and used healing procedure is then calculated as:

$$\eta_{\text{heal}} = \frac{X_{\text{heal}} - X_{\text{dam}}}{X_0 - X_{\text{dam}}}$$

The healing rate can be studied by measuring the functional properties  $X(t)$  during the healing process - if the healing procedure allows this - or by performing discrete measurements of the functional properties after different healing times. Furthermore, the healing process may be studied upon the application of different intensities of applied stimuli, e.g. at different temperatures.

Care must to be exercised when assessing the properties of partially damaged material specimens. For the mechanical properties, locally applied damage may only have a small effect on the global mechanical properties of the material. Figure 5 shows a number of damage locations and sizes and an impression of the deformation upon loading. Figure 5a shows a specimen that is cut in the middle, leaving the sides of the specimen attached. In published work, it was demonstrated that severing the cross-section of the specimen for 40%, resulted in a 12% decrease of the storage modulus and a decrease of 16% of the Young's modulus  $E$  [43]. Perforations would be almost invisible in the measured moduli, however, they would result in earlier failure upon destructive testing until failure. The same is true for the properties after healing of the damage. Some residual damage may go unnoticed, depending on the way the properties are studied.

In the same publication it was shown that the Young's modulus is recovered quickly at low stresses and strains, however the stress and strain until which the properties are recovered depend on the healing time, as shown in Figure 6(left) [43]. Healing for even longer times resulted in the recovery of the moduli until up to 30 % strain. For this reason, measuring the storage modulus is not quantitative for the healing efficiency, as it only measures the properties at very small oscillatory strains. Hence, for the mechanical properties it is important to test the material specimens until failure, or at least until a relevant stress and strain, and to compare the toughness of the material specimen, before damage, after damage and after healing, as this is the total deformation energy that can be undergone by the material specimen. This is clear from the example in Figure 6(right) where the Young's modulus

(measured at low strains) is almost completely recovered, while the stress and strain recovered only about 50 % and consequently the material toughness recovery is limited to 20 % or less [43].

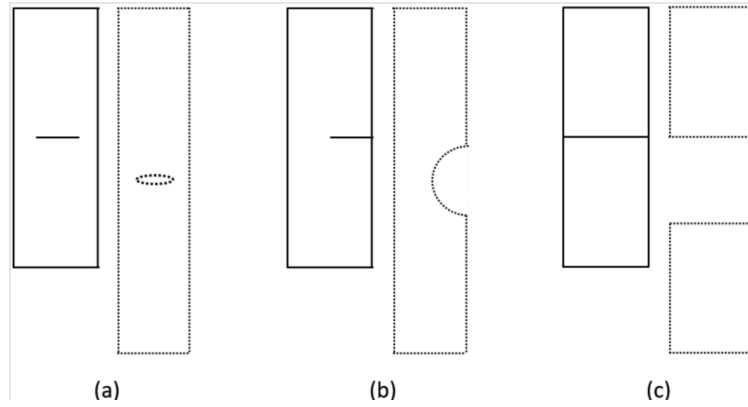


**Figure 5 Damage types: (a) incision in the middle of the specimen, (b) incision from one side of the specimen and (c) failure over the entire cross-section. Damage types are shown in relaxed (solid contours) and strained (dotted contours) states [43].**

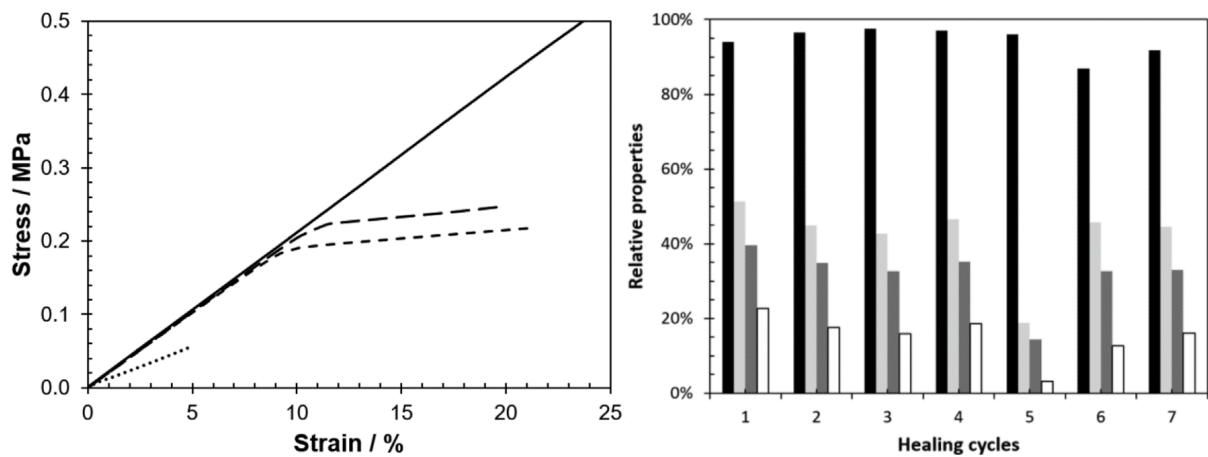


**Figure 6 (left): Stress-strain curves prior to damage (solid line), after damage (dotted line) and after two consecutive healing cycles of 48 h (long dashed line) and 45 h (short dashed line) [43].**

### 3. Results and discussion

#### 3.1. Hydrogen-bonded supramolecular networks (SupraPolix)

##### 3.1.1. Supramolecular materials

Polymers are synthesized using polyurethane-type chemistry. Typically, polyols, diisocyanate, isocytosine and optional chain extenders are dried and mixed at elevated temperatures with catalysts known in the art. Two different isocytosines are being used: 6-methyl-isocytosine or 5-(2-hydroxyethyl)-6-methyl isocytosine. These compounds have been manufactured by SupraPolix in >100 kg scales and high purities (99%) and are therefore readily available internally. Polyols and diisocyanates used are all industrially available. Reaction can be performed in bulk or in concentrated solutions (only Class III solvents), all depending on the specific formulations.

Reaction progress is followed by monitoring the isocyanate consumption with FT-IR spectrometry (NCO-vibration around  $2270\text{ cm}^{-1}$ ) and possibly by the molar mass increase using size exclusion chromatography (SEC). After isolation of the polymeric material, product quality is assessed with FT-IR, NMR and SEC for polymer identity and molecular weight and with GC-MS and LC-MS (optionally ICP-OES) for residuals determination. Polymer specification comprises identity confirmation, specific  $M_n$  and  $M_w$ -ranges, total organic residuals below 5000 ppm, and metal-catalysts below 150 ppm.

##### 3.1.2. Functional hybrid supramolecular materials

Supramolecular polymers as obtained under section 3.1.1 have been modified with carbon black particles to render them electrically conductive or with neodymium alloy powder in order to introduce magnetic properties.

This has been performed in a post-processing procedure using a twin-screw extruder. First a masterbatch has been made by mixing the supramolecular polymer dissolved in a chloroform/ethanol mixture with the selected functional solids in the desired amounts by stirring. This formulation was subsequently dried and cut in small pieces that were fed into a double screw extruder operating at  $140\text{ }^\circ\text{C}$ . Typical loadings for carbon black are 25 - 35 w% and for Neodymium 30 – 70 w%.

Ensaco 260G has been used as source for the carbon black powder as it combines high conductivity with acceptable processing performance. It is obtained from Imerys Graphite and Carbon, it has a BET nitrogen surface of  $65\text{ m}^2/\text{g}$  and sieve residue  $45\text{ }\mu\text{m}$  is 2 ppm.

Neodymium powder is obtained from Magnequench, it has a  $B_r$  of 875 – 905 mT,  $(BH)_{\text{max}}$  of 102-118  $\text{kJ}/\text{m}^3$  and  $D_{90} < 10\text{ }\mu\text{m}$ .

#### 3.2. Diels-Alder-based networks (VUB)

##### 3.2.1. Thermally reversible dissociative networks

###### 3.2.1.a. Monomer functionalization and reactivity

Any amine (e.g. a1 and a2 in Figure 7) can be functionalized with furan functional groups using the irreversible epoxy-amine reaction, according to the synthesis route published in 2011 [44], and adopted and adapted by many researchers since. The epoxy-amine **functionalization** can be carried out to near 100% completion, as evidenced by TGA, showing no loss of the volatile furfuryl glycidyl ether (FGE, b), and by FTIR and  $^1\text{H}$ NMR spectroscopy, showing the complete consumption of the epoxide rings by the amine groups. Furthermore,  $^1\text{H}$ NMR spectroscopy is then used to calculate the number of furan functional groups of the newly formed monomer, its structural molar mass and the functional weight (= molar mass divided by the number of functional groups) (details in [44]).

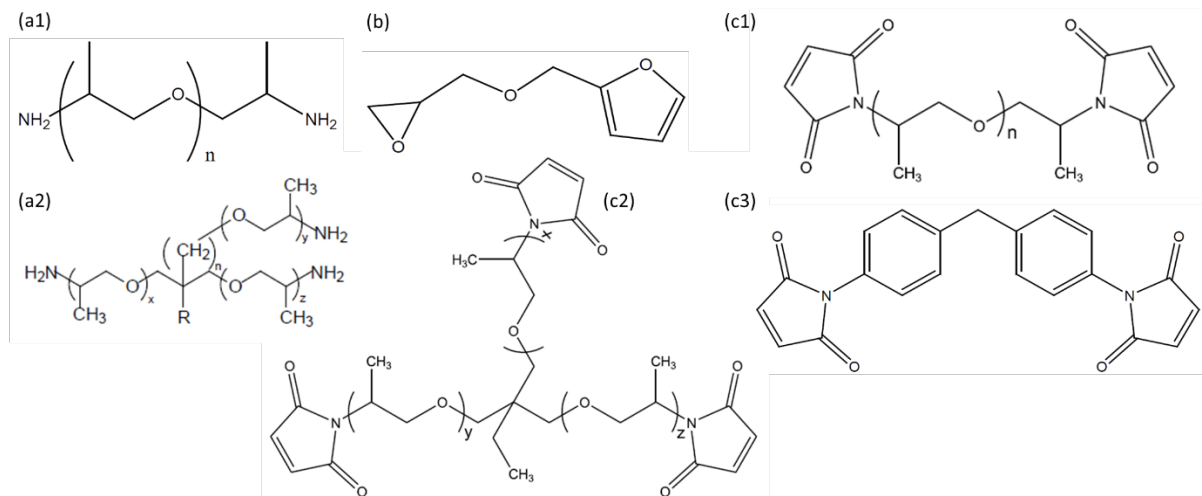


**Figure 7: Jeffamine amine hardeners (a1 and a2) are functionalized with furfuryl glycidyl ether (b) to create polyfuranic compounds that are subsequently reversibly crosslinked using maleimides (c1, c2 and c3).**

The **reactivity** of the functional groups of the monomers is studied using FTIR spectroscopy [45,46], <sup>1</sup>HNMR spectroscopy (Figure 9 [33]) or calorimetry (Figure 8 [33,36–38]), following the protocol detailed in section 2.2.1. The obtained kinetic parameters (pre-exponential factors  $A_i$  and activation energies  $E_i$ ) can then be used to calculate the reaction rate constants  $k_i$  to simulate the changes in the chemical structure as a function of temperature  $T$  and time  $t$  and as a function of the choice of monomers (functional weights, or inversely, concentrations of functional groups  $[F]$  and  $[M]$ ):

$$k_i = A_i e^{-\frac{E_i}{RT}}$$

$$v = \frac{d[A_{\text{endo}}]}{dt} + \frac{d[A_{\text{exo}}]}{dt} = k_{\text{DA,endo}}[F][M] + k_{\text{DA,exo}}[F][M] - k_{\text{rDA,endo}}[A_{\text{endo}}] - k_{\text{rDA,exo}}[A_{\text{exo}}]$$

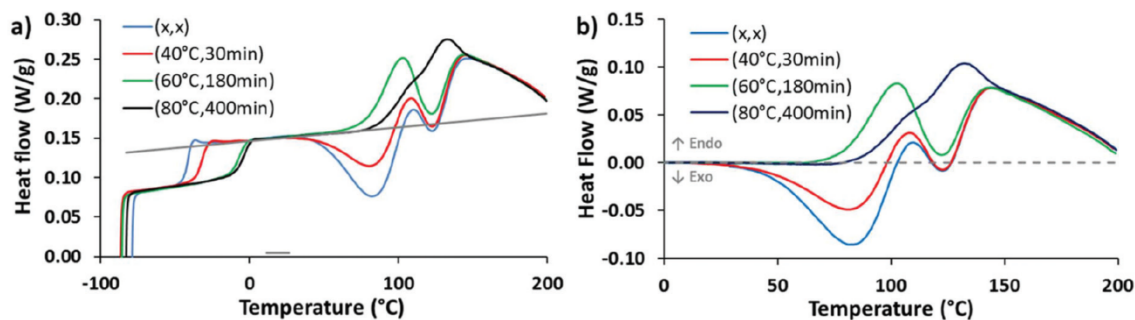


**Figure 8: DSC thermograms of the heating step after ( $T_{\text{iso}}$ ,  $t_{\text{iso}}$ ) temperature treatment for a F400–M400 ( $r=1$ ) system: (a) experimental heat flow curves showing the glass transition temperature and exothermic adduct formation and/or endothermic adduct dissociation, and (b) after subtraction of the glass transition step and baseline for kinetic modelling [33].**

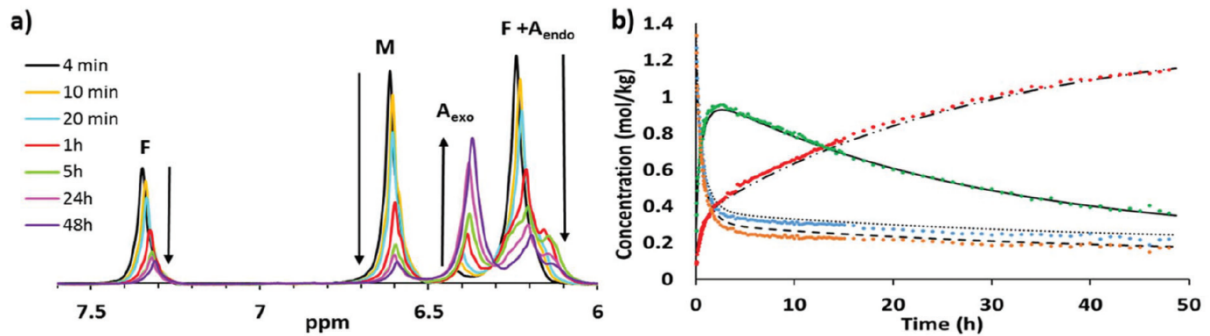


**Figure 9: The reaction of FGE and M400 in PPG425 at 56.6 °C: (a)  $^1\text{H}$  NMR spectra, showing the evolution of resonance peaks of furan, maleimide and both adducts and (b) the  $^1\text{H}$  NMR concentration profiles, compared to those simulated from calorimetry [33].**

The **critical gel conversion**  $x_{\text{gel}}$  at which the reactive monomer mixture forms an incipient polymer network structure depends on the functionalities of the monomers  $f_F$  and  $f_M$ , and maleimide-to-furan ratio  $r = [M_0]/[F_0]$  according to the Flory-Stockmayer equation [47]. The gel time  $t_{\text{gel}} = t(x=x_{\text{gel}})$  in turn depends on the reactivity of the functional groups and the temperature [46], as shown in Figure 10. The time to reach near completion of the reaction (near equilibrium conditions at a certain temperature) can also be calculated using the kinetic parameters, as performed for the study of the influence of the stereochemistry of the Diels-Alder reaction [33]. Doing so the curing temperature profile can be optimized to minimize the time necessary to achieve near complete network formation.

$$x_{\text{gel}} = \frac{1}{\sqrt{r(f_F - 1)(f_M - 1)}}$$

The **reversible (equilibrium) gel transition** temperature  $T_{\text{gel,eq}} = T(x_{\text{eq}}=x_{\text{gel}})$  further depends on the position of the reaction equilibrium, which in turn depends on the concentrations of functional groups [F] and [M] [48], as shown in Figure 11.

### 3.2.1.b. Thermoreversible polymer network formation

The **viscoelastic properties** of the thermoreversible polymer networks are studied using dynamic rheometry and dynamic mechanical analysis (DMA). The network formation (Figure 10) and network dissociation (Figure 11 and Figure 13) can be studied as a function of time and temperature to be related to the chemical structure build-up, simulated using the kinetic parameters, established in 3.2.1.a. The **gel point** is defined as the point at which the loss angle curves intersect [39]. It can be measured isothermally, starting from an unreacted mixture (**gelation**), in cooling (gelation), or in heating (**degelation**), in either continuous heating/cooling, or in stepwise conditions, with steps long enough to reach equilibrium.

In the liquid state (before gelation), the variation of the **viscosity** of the reactive monomer/oligomer mixture can be related to variation of the molecular weight averages and distributions, which in turn depend on the extent of reaction. Such information can be used to simulate the material behaviour during **manufacturing processes** such as filament extrusion and fused filament fabrication (FFF) using the extruded filaments to optimize the processing conditions to achieve the best results [40]. The temperatures in the different heated zones (Figure 9) in the filament extruder were optimized to (i) retain sufficient pressure from the screw to push the material through the extruder, (ii) achieve the necessary flow behaviour to achieve a continuous filament and (iii) optimized residence time and cooling rate to achieve a solid filament with consistent diameter and smooth surface finish.

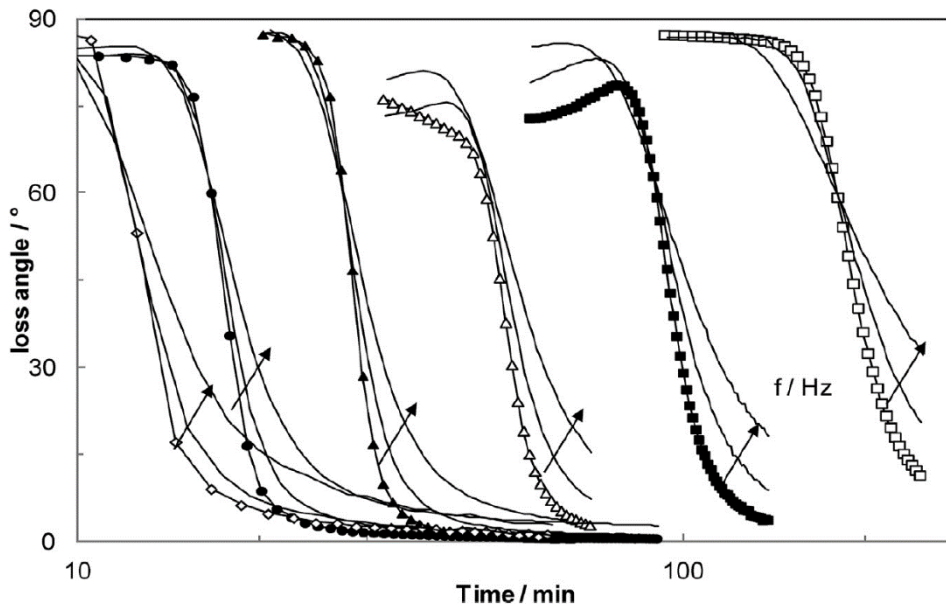


Figure 10 Isothermal network formation (gelation) of M400-F400, studied using multifrequency dynamic rheometry experiments at temperatures ranging from 30 °C (longest gel time) up to 80 °C (shortest gel time) [46].

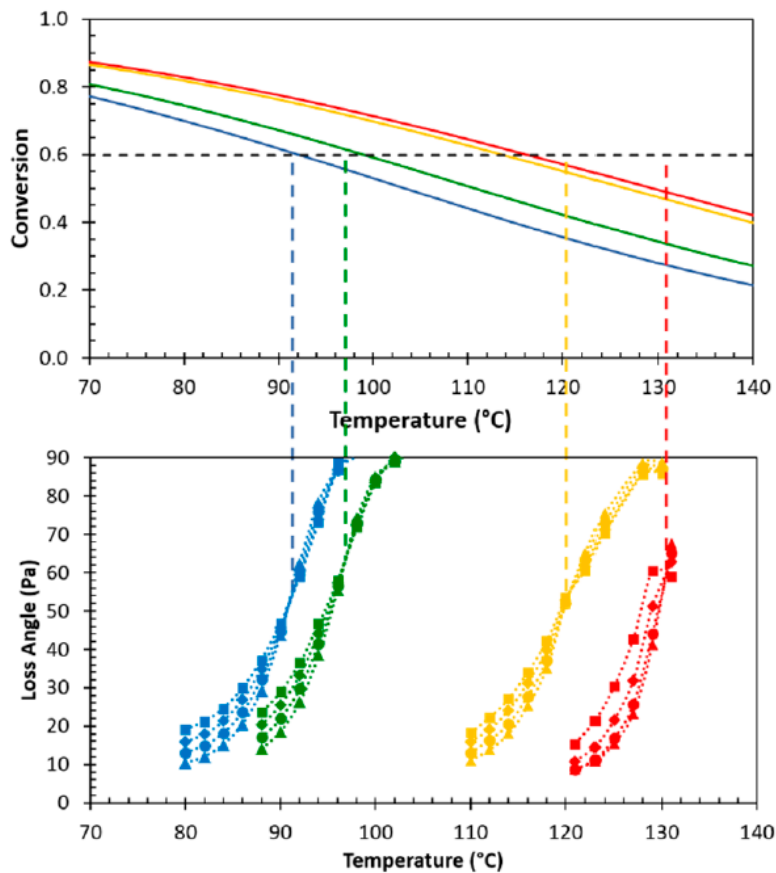
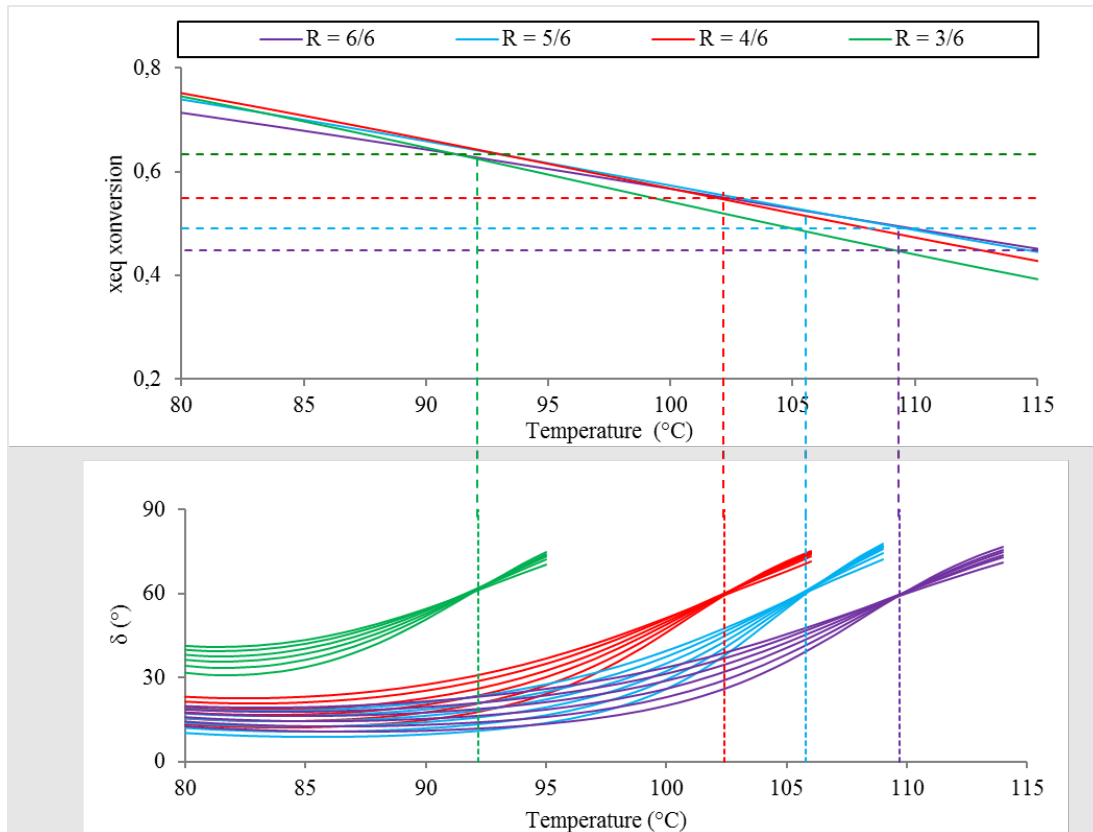
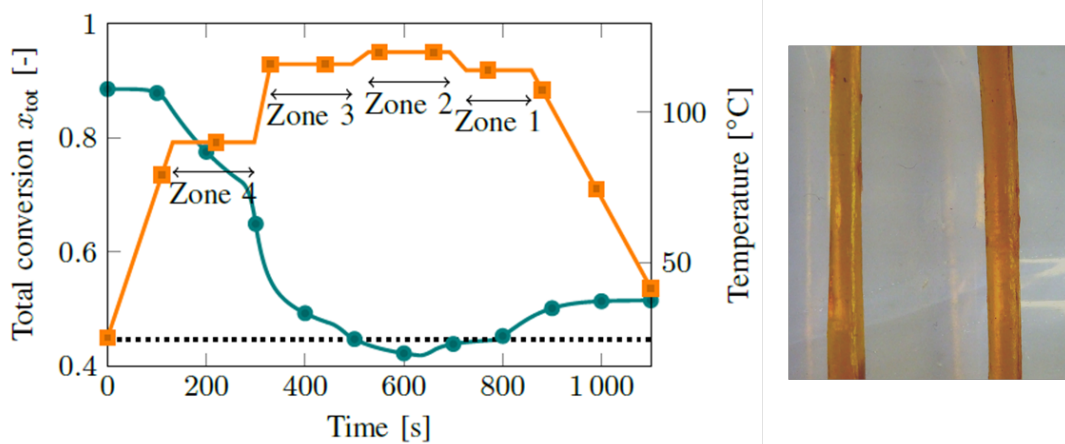


Figure 11 Thermal dissociation (degelation) of DPBM-F4000 (blue), -F2000 (green), -F400 (yellow) and -F230 (red), studied using dynamic rheometry, related to equilibrium conversion simulations [48].



**Figure 12: Thermal dissociation (degelation) of different DPBM-F5000 materials that differ in  $r$ -values, studied using dynamic rheometry, related to equilibrium conversion simulations (figure based on data in [49–51]).**



**Figure 13 Temperature profile during extrusion of DPBM-F5000 ( $r=1$ ) showing different heated zones to achieve smooth and consistent filaments (right) [40].**

### 3.2.1.c. Glass transition determination using DSC

The **glass transition** temperature  $T_g$  can be related to the reaction conversion according to the Di Benedetto equation [52], with  $T_{g0}$  the  $T_g$  of the unreacted system at  $x = 0$  and  $T_{g1}$  the  $T_g$  of the fully reacted system at  $x = 1$  and  $\lambda$  an optimization parameter, which is often close to the ratio between the heat capacity changes  $\Delta C_p$  of the fully reacted system to that of the unreacted system.

$$T_g = T_{g0} + \frac{\lambda x}{1 - (1 - \lambda)x} (T_{g1} - T_{g0})$$

$$\lambda = \frac{\Delta C_{p1}}{\Delta C_{p0}}$$

This information is especially important for the study of the reaction kinetics in thermosetting systems that vitrify under the studied reaction conditions, resulting in drastically reduced reaction rates upon vitrification due to the diffusion-controlled reaction conditions [36–38]. The  $T_{g0}$  and  $T_{g1}$  depend on the choice of monomers (Figure 7) to construct the thermoreversible polymer network.

The  $T_g$  of the Diels-Alder networks was determined using DSC (Figure 14) and DMA (section 3.2.1.e). At the glass transition, the segmental chain mobility increases (in heating), resulting in an increase in heat capacity, visible as a step in endothermic direction in the heat flow signal. An increase in concentration of reversible adducts, and therefore crosslink density, leads to a decrease in flexibility in the network, which can be observed as an increase in  $T_g$ . According to the measurements done on the Diels-Alder networks, this increase in  $T_g$  with an increase of maleimide concentration is more pronounced for higher concentrations. At low concentration, an increase in initial maleimide concentration has a very limited influence on  $T_g$  (limited difference between DPBM-FT5000 materials with different stoichiometric ratios  $r$ ). This is because at low crosslink density the flexibility of the connecting chains is the main controlling parameter.

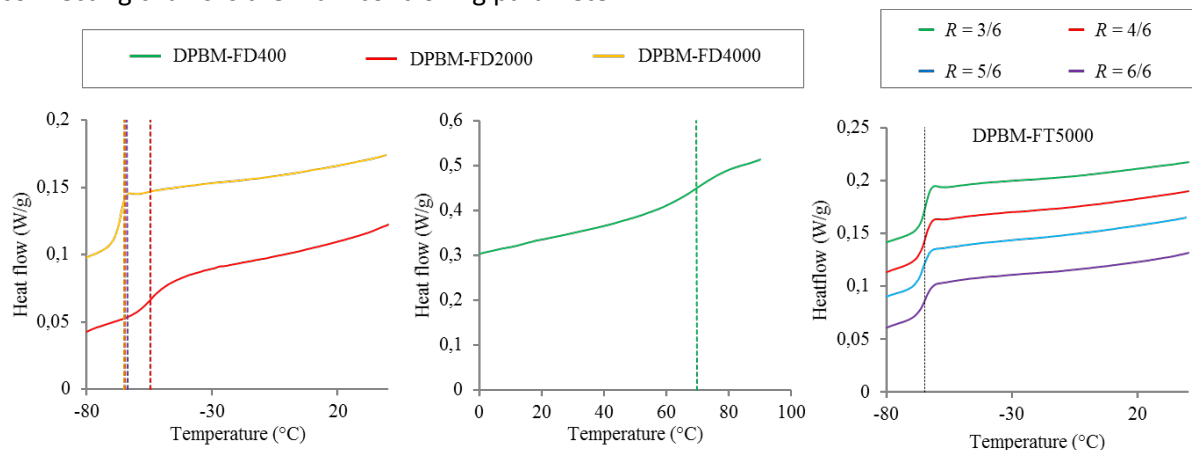


**Figure 14 DSC-measurements at a heating rate of 5 K min<sup>-1</sup> showing the glass transitions of several Diels-Alder networks.**

### 3.2.1.d. Stress-strain behaviour

The mechanical behaviour of the reversible polymer networks was characterized following the protocols described in section 2.3. **Stress-strain** curves have been recorded for all developed self-healing materials at different deformation rates. Examples of these experiments are presented in Figure 15 and in [49,50,53,54]. These tensile tests illustrate that by varying the network composition,

e.g., changing the molar weight of the monomers, their functionality or the ratio between them, large variations in mechanical behaviour can be achieved. For elastomeric DA-networks ( $T_g < T_{\text{application}}$ ) strains at fracture of 150 % or higher can be reached (Figure 15A and C). This allows using these materials for soft robotic applications [28,49,50,53]. Higher concentrations result in higher crosslinking densities, which increases the fracture stress, as upon fracture more crosslinks have to be broken. For networks with a  $T_g$  above application temperature, very small strains at fracture (Figure 15B) are observed, since the mobility of the chains is highly restricted (only vibrational motions are available), which also leads to a much higher Young's modulus (1.90 GPa). This thermoset was used to construct a self-healing mechanical fuse, which can be inserted in a soft actuator to act as a sacrificial healable component that protects the system against overloads and high impacts [54].

Most of the measurements have been performed in **tension**, while recently also other deformation modes, such as compression and torsion, are being used to complete the modelling of the **hyperelastic behaviour** of the thermoreversible polymer networks. At this stage of the project, the hyperelastic behaviour is modelled using a Neo-Hookean constitutive law based on both tension and compression data. The fitted constitutive law is being used in finite element method (FEM) modelling, in both the Abaqus and SOFA environment, to simulate the actuator deformation and contact forces with external objects. This is currently performed non-real time and is used in the design phase of the new self-healing actuator geometries. In a later phase of the project, the FEM models will be used as a base for real time controllers for actuation. Moreover, the knowledge on the influence of the network composition on the mechanical properties of the Diels-Alder network is used for the optimization the material properties for the intended applications.

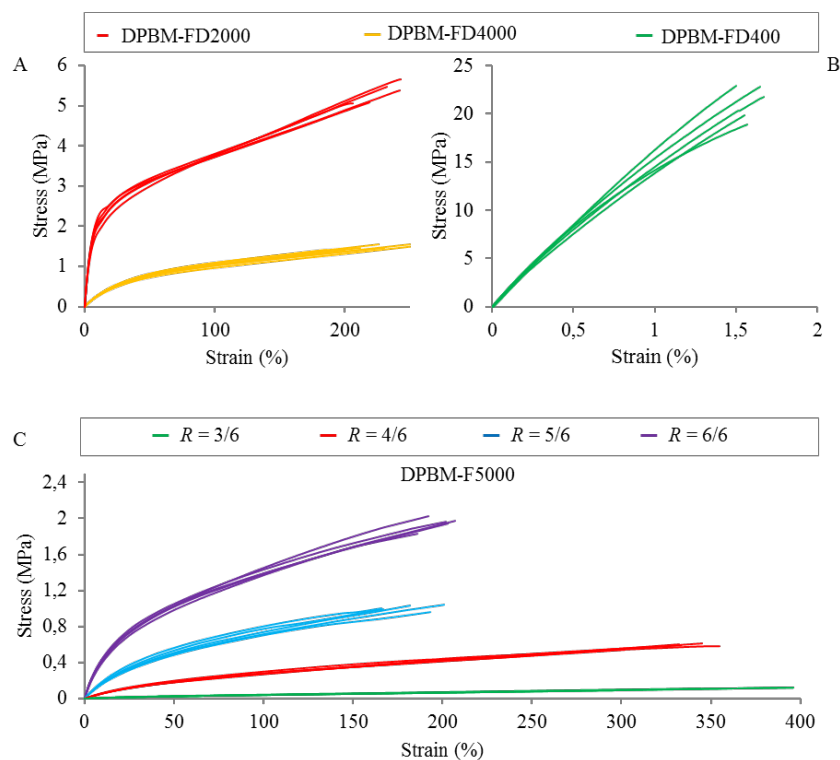


**Figure 15** Static stress-strain tensile testing until fracture. **A)** Diamine based Diels-Alder elastomers. Stress-strain tensile test is performed at  $1\% \cdot s^{-1}$  and  $25\text{ }^\circ\text{C}$  [53]. **B)** Diamine based Diels-Alder thermoset. Stress-strain tensile test is performed at  $1\% \cdot \text{min}^{-1}$  [54]. **C)** Triamine based Diels-Alder elastomers. Stress-strain tests are performed at  $1\% \cdot s^{-1}$  and  $25\text{ }^\circ\text{C}$  [49,50]. Engineering stresses and strains are displayed.

Cyclic stress-strain experiments are performed to study the mechanical hysteresis, the **Mullins effect** [55] and the **elastic recovery**. Dynamic strain sweeps are performed for the elastomers and composites to study the **Payne effect** [56]. Strain sweeps are performed with different relaxation times between consecutive sweeps to follow the elastic recovery of the elastomers and composites.

### 3.2.1.e. Visco-elastic behaviour of solids

The **viscoelastic behaviour** was measured by DMA over a temperature range from -80 °C to 100 °C, using strain amplitudes of 0.2 % and a frequency of 1 Hz, with a rate of 1 K min<sup>-1</sup> (Figure 16). When increasing the temperature above  $T_g$ , all DA-networks show a clear drop in mechanical properties (storage and loss modulus), due to an increase in mobility when passing the glass transition region. In DMA,  $T_g$  is commonly defined as the temperature where the loss modulus ( $E''$ ) reaches a maximum. These DMA results nearly coincide with the  $T_g$  determination through DSC. Small differences in temperature between the  $T_g$  determined in DSC and DMA are due to the difference in measurement approach and larger thermal gradients and thermal lag in the DMA compared to the DSC.

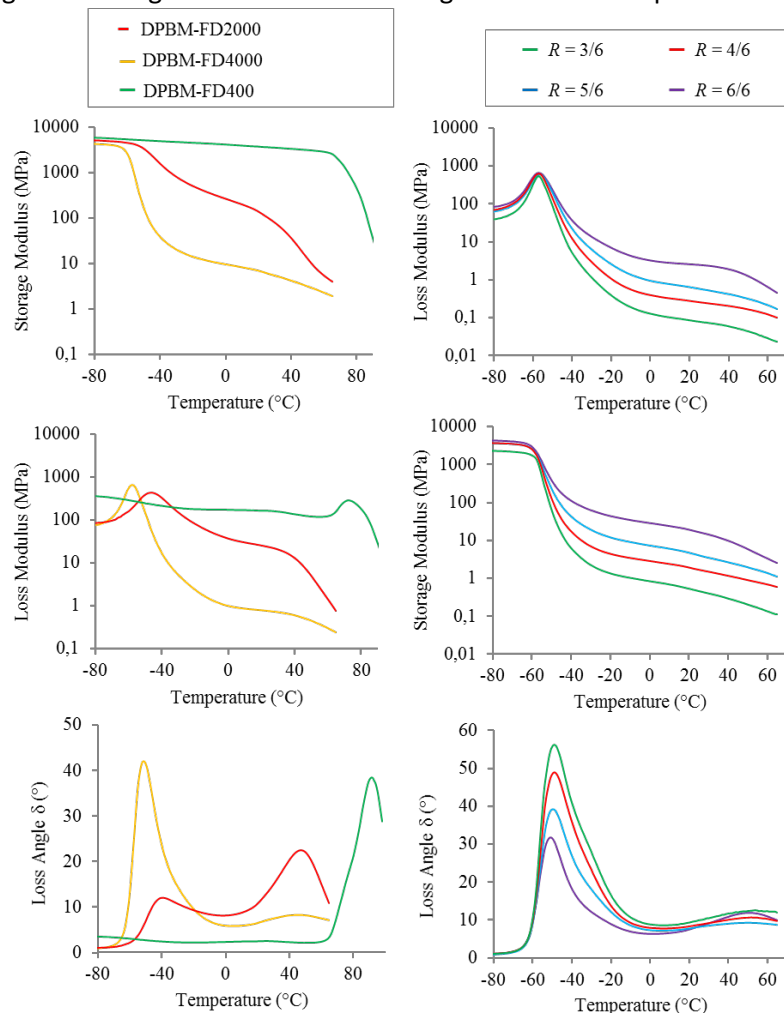


**Figure 16: DMA-measurements performed in a temperature window of -80 to 100 °C with a temperature ramp of 1 K min<sup>-1</sup> and an oscillating strain with amplitudes of 0.2 % and a frequency of 1 Hz. From the measured oscillating stress the storage modulus ( $E'$ ), loss modulus ( $E''$ ) and loss angle ( $\delta$ ) can be derived. The  $T_g$  is defined as the temperature at which the loss modulus ( $E''$ ) reaches a local maximum.**

In contrast to irreversible polymer networks, the moduli do not show a rubber plateau of constant or slightly increasing storage modulus upon heating above  $T_g$ . Instead, the storage and loss modulus gradually decrease, because upon heating the retro-DA-reaction is more and more favoured and the crosslink density gradually decreases. This illustrates the reversibility of the DA-crosslinks. Depending on the position of its  $T_g$ , the DA-network will exhibit a brittle glassy behaviour (if  $T_g > T_{\text{application}}$ ) or a flexible elastomeric behaviour (if  $T_g < T_{\text{application}}$ ). DA-networks with a high initial maleimide concentration and high crosslink density will have a  $T_g$  higher than application temperature. The DPBM-F400, for example, has a  $T_g$  at 72.2 °C and therefore exhibits an almost entirely energy elastic, glassy behaviour at 25 °C, illustrated by a high storage modulus (3.6 GPa), a relatively low loss modulus (164 MPa) and a very low loss angle of only 3°. The DPBM-F4000 on the other hand has a much lower  $T_g$  at -57.8 °C, due to a lower initial concentration of maleimide and lower crosslink density and the higher relative content of flexible PPO chains. At room temperature it behaves like a flexible rubber, with low storage modulus (6.1 MPa), a relatively low loss modulus of (0.76 MPa), and a low loss angle of 7°. This non-negligible loss angle indicates that a viscous component is present in the mechanical response, however, it is limited. This high contrast in mechanical properties illustrates that the network design parameters allow synthesizing very brittle, stiff self-healing materials, as well as very flexible, rubbery self-healing materials.

Many different thermoreversible polymer networks have been evaluated for **soft robotics applications**. Dedicated tests and testbenches have been developed and used to characterize a self-healing sacrificial mechanical fuse [54], pneumatically actuated cells [57] for pressure-actuated robotic hands and grippers [50,53] and muscles [58], a tendon-driven gripper [49] and a passive gripper [40].

### 3.2.1.f. Stress relaxation

**Stress relaxation** experiments were conducted using a DHR-2 dynamic rheometer (TA Instruments, USA) in shear mode on samples with a 15 mm diameter (parallel plates), applying strains varying between 1% and 50%. The dwell time each temperature was adapted using the reaction kinetics model to reach full relaxation, at least for the measurements at elevated temperatures. A model was fitted to the stress relaxation experiments, taking into account all experiments at different temperatures. Figure 17 (left) shows stress relaxation experiments performed at different temperatures at 1% strain, for which the highest temperature was too close to the gel point temperature of the material. Figure 17 (right) compares the temperature dependence of the stress relaxation time constant for different material compositions.

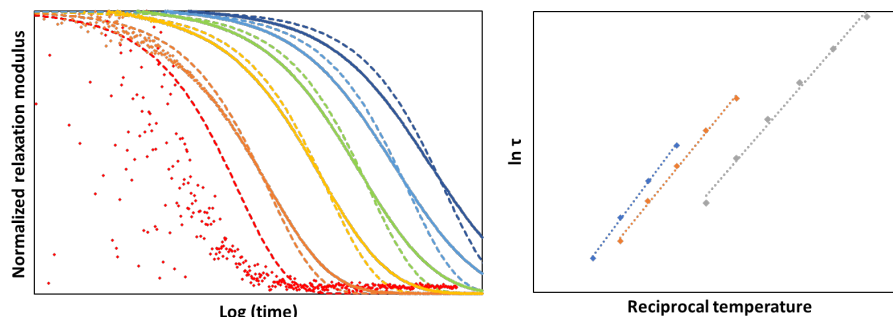


**Figure 17 (left) Normalized relaxation modulus at different temperatures, fitted with an exponential decay to determine the time constants and (right) the time constants as a function of the reciprocal temperature for different thermoreversible polymer networks. The dashed lines represent model fits [unpublished data presented as an example for the stress relaxation study].**

Using this information, it could be calculated that it would take several years at 25 °C to relax the stress resulting to the 1% strain deformation. In addition, stress relaxation has been studied at different magnitudes of deformation (1%, 10%, 20% and 50%) to evaluate the different processes contributing to the stress relaxation phenomenon.

**Creep experiments** were performed using a Q800 DMA (TA Instruments, USA) in tension on rectangular samples (10 mm × 5.5 mm × 1 mm). Cyclic creep experiments were performed at different temperatures with alternating loading of the samples for a fixed time (typically 1 h), followed by a relaxation period for a fixed time, double that of the loading cycle.

### 3.2.1.c. Self-healing behaviour

The self-healing ability of the reversible Diels-Alder networks was studied following the protocols described in section 2.7. This is illustrated in this report through the influence on the mechanical properties of DPBM-FD4000 of repeated cycles of healing by heating and the subsequent recovery [53]. To do so, six series of four samples each were prepared for two different batches of the DPBM-FD4000 polymer. All samples, except the reference series, were subjected to a heating procedure (4 hours at 80 °C, followed by at least 3 days at 25 °C), which can be considered the equivalent of six SH procedures based on the length of the normal isothermal step, which has a duration of 40 min (Figure 18). For one series, this heating procedure was performed once, for the next twice, for the third thrice, etc., giving an equivalent of 0, 6, 12, 18, 24, and 30 SH-cycles. For each series, DMA was used to measure the storage modulus ( $E'$ ), loss modulus ( $E''$ ),  $\tan(\delta)$ , and the glass transition temperature ( $T_g$ ) (Figure 18).

For every 4 hours spent at 80 °C, the equivalent of six SH cycles,  $E'$ ,  $E''$  and  $\tan(\delta)$  lower a bit, whereas the  $T_g$  remains more or less the same (Figure 18). The reproducibility of the observed decreasing trends was shown by the similarity between the results of batches 1 and 2. The small drop might point to a limited decrease in crosslink density resulting from the formation of irreversible bonds through side reactions in the network, such as the Michael addition of amine impurities to maleimide groups and the homopolymerization of bismaleimide, both typically occurring at higher temperatures. These side reactions imply that some of the furan functionalities can no longer form a DA-bond, resulting in a gradual decrease of the crosslink density and modulus after healing. The **recovery efficiency**, defined as  $(E'_{\text{initial}} - E'_{\text{xSH-cycles}})/E'_{\text{initial}}$  is, on average, 93.4% for one 4-hour heating cycle (Figure 18). Projecting this to a 40 min SH-cycle, a very high recovery efficiency of 98 to 99% is reached. The small increase in flexibility results in the small increase in the contraction force of the PPAM actuator observed for the second and third SH cycles (Figure 18). The author believes that the Michael addition has the largest influence, because this reaction occurs at lower temperatures compared to maleimide homopolymerization. The recovery efficiency can be increased by working with a bismaleimide with higher purity and by avoiding the presence of unreacted amine, reducing the probability of Michael addition reactions.

Aside from the recovery of the mechanical properties mentioned above, the recovery of the mechanical strength is extremely important. Consequently, the fracture properties of pristine samples and healed samples, measured in stress-strain tensile tests, are compared for the different Diels-Alder materials. The characterisation is illustrated in this report using a Diels-Alder material, DPBM-FT5000-r0.5, that can autonomously heal macroscopic damages at application temperature and does not require heat for healing [28]. However, due to the slow kinetics of the Diels-Alder at application temperature (around 25 °C), the healing takes time. Samples with a width of 5.5 mm and a thickness of 2 – 2.5 mm (Figure 19A) were subjected to stress–strain tensile tests until they fractured. For reference, six (undamaged) samples were fractured in a stress–strain test (Figure 20A). These samples failed, on average, at an approximate strain of 245% and a stress of 0.1 MPa.

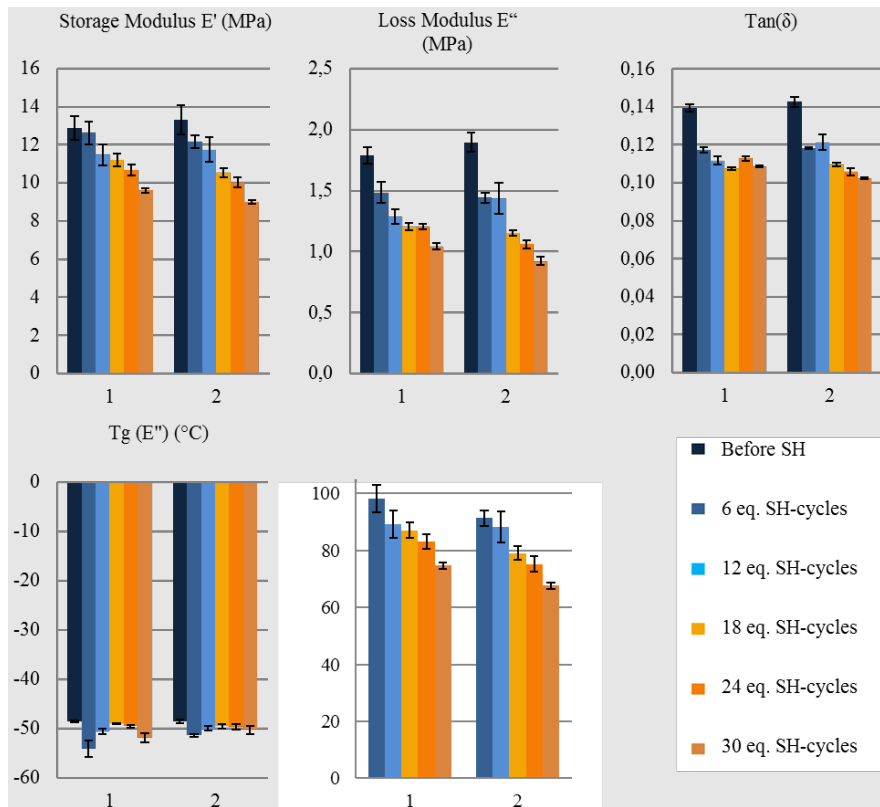


**Figure 18 Influence of the heating procedure (4 hours at 80 °C followed by at least 3 days at 25 °C) on the viscoelastic properties expressed in equivalent SH cycles. Two batches 1 and 2 were analysed using DMA with a temperature ramp of 1 Kmin<sup>-1</sup>, a frequency of 1 Hz and strain amplitude of 0.2%. The error bars represent the standard error of the mean (SEM) [53].**

Next, 24 samples were sliced in two using a clean scalpel blade (Figure 19B). Immediately after cutting, the two ends were brought back in contact manually. When macroscopic misalignments are avoided while fitting the fracture surfaces back together, the instant healability of the DPBM-FT5000-r0.5 network allows to precisely merge the parts together, such that the cut is no longer visible (Figure 19C). These samples were left to heal at room temperature for 1 day, 3 days, 7 days, or 14 days. For each healing time, 6 samples were fractured in a stress-strain test (Figure 20A, 1 %·s<sup>-1</sup>).

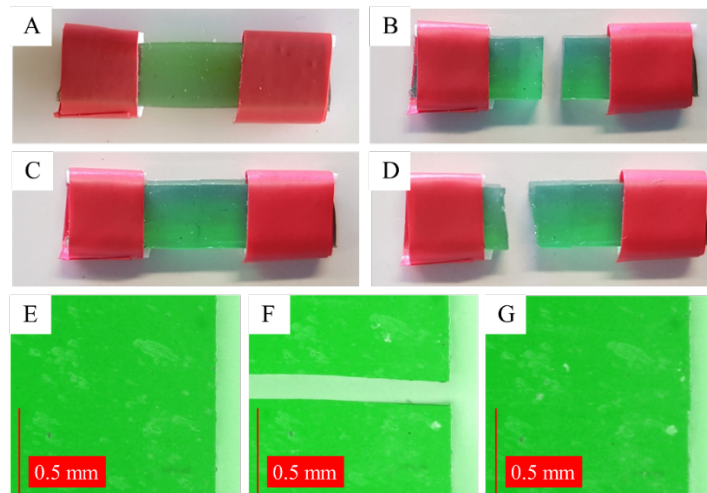


**Figure 19 Testing of autonomous healing at room temperature. A) Samples with a width of 5.5 mm, a thickness of 2-2.5 mm, and a length of 8-10 mm. B) Samples are sliced in two using a scalpel blade. C) Samples are pressed back together seconds after damage and placed at room temperature for 1 day, 3 days, 7 days, or 14 days before being subjected to a stress-strain tensile test until fracture. D) The samples that were cured for 14 days do not fracture on the location of the initial damage but on a new location [51].**

The mean fracture stresses and strains are presented in the block diagrams in Figure 20B. In Figure 20C, the mean healing efficiencies for the different healing times ( $Ht$ ) were calculated by comparing the fracture strains and stresses with those measured in the reference experiment:

$$\eta_{\epsilon(Ht)} = \epsilon_{fract(Ht)} / \epsilon_{fract(not\ damaged)}$$

$$\eta_{\sigma(Ht)} = \sigma_{fract(Ht)} / \sigma_{fract(not\ damaged)}$$

Figure 20A illustrates that after healing at room temperature very similar stress-strain characteristics are measured, but failure occurs at much lower stresses. Creating the interfacial DA-bonds clearly takes time, which is due to slow reaction kinetics and network mobility. After healing for 1 day at 25 °C only 50% of the fracture stress ( $\eta_{\sigma}$ ) is recovered (Figure 20C). Visual inspection showed that the fracture took place at the same location as where the cut was made previously. The formed fracture surfaces looked again clean and identical to the picture in Figure 19B. The healing efficiencies ( $\eta_{\epsilon}$  and  $\eta_{\sigma}$ ) can be increased by prolonging the healing time. Indeed, after 3 days, 7 days, and 14 days, the fracture stress has recovered by respectively 62%, 91%, and 97%. After 14 days of healing at room temperature, the fracture did no longer take place at the location where the cut was made, but rather at a location where an imperfection causes stress concentrations (e.g., a cavity caused by a solvent bubble or a dust particle, Figure 19D). Taking into account the standard deviations of the mean (SEM) presented on the block diagrams in Figure 20C and the fact that fracture does not take place at the location of the “scar” of the cut, it can be concluded that after 14 days, the cuts are completely healed and that the initial strength of the samples has been recovered completely.

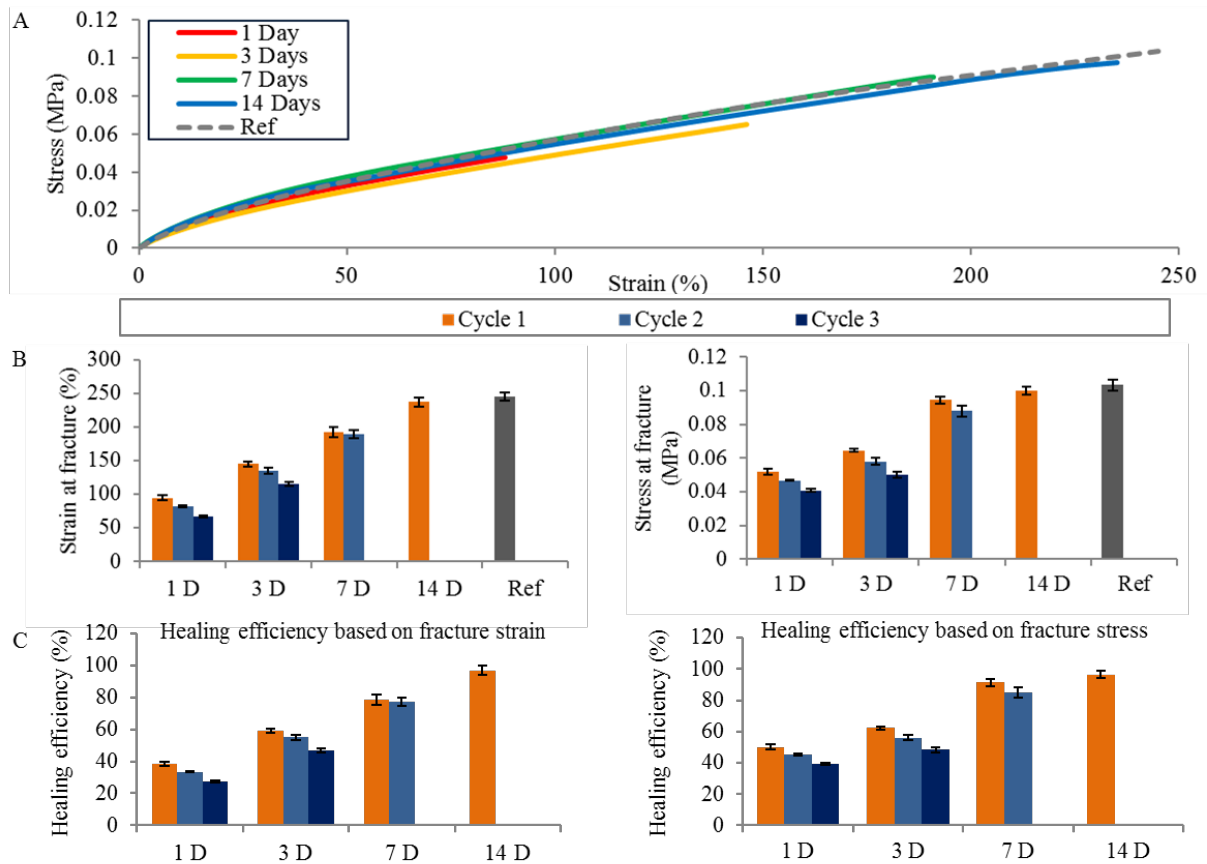


**Figure 20: A) Comparison of stress-strain curves of reference (undamaged) samples and samples that were cut all the way through and subsequently healed at room temperature for 1 day, 3 days, 7 days and 14 days. Stress-strain tests are performed with a strain ramp of 1 %s<sup>-1</sup>. B) Mean values (of 6 samples) of the strain and stress at fracture, derived through tensile testing, are presented for the reference sample and samples that are healed for 1 day, 3 days, 7 days and 14 days at 25 °C. C) Healing efficiencies based on the fracture strain and fractures stresses of the healed samples relative to fracture parameters of the reference samples. Error bars represent the standard error of the mean (SEM) [51].**

For the samples that were healed for 1 day, 3 days, and 7 days, immediately after fracturing the samples in the stress-strain tensile test to test the healing efficiency, the generated two pieces (Figure 19B) were pressed back together to heal (Figure 19C). After again healing for the same duration, 1 day, 3 days and 7 days, the samples were fractured once more in the tensile tests. For all healing times, the fracture strain and fracture stress of the second healing cycle is slightly lower (Figure 20B). A possible explanation is that at the surface of cavities, generated at the merging zone, the amount of available reactive maleimide and furan groups decreases slowly as a function of time. After intermediate healing times of 1 day, 3 days, and 7 days, not all cavities are completely sealed. Consequently, when broken in the subsequent stress-strain tensile test, the resulting fracture surfaces have less reactive components on their surface compared to the fracture surfaces generated by cutting a fresh sample. As a result, the recovery of fracture strain and fracture stress will take longer in the second healing cycle. In addition, the cavities that remained after incomplete healing can be enlarged in the first stress strain test before rupture occurs. When the two parts are placed back together for the second healing cycle, the surfaces are probably matching less well, and the cavities are slightly bigger than in the first healing cycle. As a result, more extensive “zipping” is required, increasing the required duration of the

healing process. For the same reasons the recovery of the initial properties in the third healing cycle is even lower than for the second. Although not yet experimentally validated, it is thought that even when fracturing a sample before all cavities are healed (e.g. after 1 day), a complete recovery of that sample can still be achieved in a subsequent longer healing cycle (e.g. > 14 days).

In addition to healing experiments of the materials upon controlled damage, the damage-healing capabilities of various thermoreversible polymer networks have been evaluated in 3D structures for **soft robotics applications**. The actuator components have been damaged in controlled fashions through manually applied cuts and perforations, as well as overloading of the sacrificial mechanical fuse [54], overpressure for the pneumatic actuators [50,53,57,58], delamination of bonding interfaces [49,50] and complete severing of a part of the actuator [40,49,50].

### 3.2.2. Electrically conductive materials

Many electrically conductive thermoreversible polymer networks have been prepared and studied, varying (i) the flexibility of the polymer matrix by changing the concentration of maleimide groups [M] as crosslinks in the network structure, (ii) the type of electrically conductive filler, and (iii) the loading content of the filler. The reactivity and reversibility were confirmed using aforementioned characterization protocols and the viscoelastic and thermomechanical properties and self-healing behaviour compared to the unfilled polymer networks.

The **electrical conductivity** of the composites was measured using a 2-point resistance measurement to determine the electrical percolation threshold. Based on this assessment, combined with the characterization of the mechanical properties, good candidates were selected to be tested in more detail. Their self-healing behaviour was studied under comparable conditions as the pure polymer matrices to allow straight-forward evaluation of the effect of the filler on the mobility required for the healing action. Good candidates were extruded into fibres and moulded into more complex shapes to create various self-healing sensor morphologies for the sensing of deformation, proximity, force, and ultimately, damage. The electromechanical characterization of the pure and embedded sensor fibres were performed following the protocol described in section 2.5.

Moreover, dedicated tests and testbenches have been developed and used to characterize the different sensors and the testbenches and related tests for the soft actuators have been adapted to allow acquisition of the sensor signal in addition to the characterization of the actuator.

## 3.3. Double dynamic networks (ESPCI)

### 3.3.1. Hybrid vitrimer network

#### 3.3.1.a. Introduction

In the following section, the characterization methods employed for the preparation of a double dynamic (hybrid vitrimer) network as self-healing material for soft robotic applications are described. The hybrid vitrimer networks studied, are physically and chemically crosslinked networks. They contain both non-covalent hydrogen bonds and covalent exchangeable  $\beta$ -hydroxy esters bonds in the same network. One of the main advantages of double dynamic networks is to combine a rapid partial self-healing at room temperature by supramolecular interactions [59–62] and exchangeable esters bonds for a complete recovery at higher temperature [63]. This combination of a rapid self-healing at low temperature and good mechanical properties brought by covalent dynamic bonds, make them promising materials for soft robotic [64]. The hybrid network is synthesized in a two-step reaction, as displayed in Figure 21. The first step is the functionalization of vegetable fatty acid oil (77 wt% of trimer) with 2-aminoethylimidazolidone (UDETA) using an amidification reaction. The second step is the formation of a chemically crosslinked network by addition of the functionalized acid on di- or tetra-





The typical procedure for the synthesis of supramolecular prepolymer SP50 is as follows: (i) Pripol 1040 (100 g, 338 mmol of COOH) and UDETA (21.8 g, 169 mmol) are introduced at room temperature in a 500 mL thermostatted reactor with a nitrogen inlet, a stirring system, and a bottom valve. (ii) The reaction is carried out for 3 h at 160 °C under N<sub>2</sub> flow. (iii) The resulting material is collected as a viscous oil through the bottom valve at 160 °C.

After each synthesis, the final conversion of carboxylic acids into amides of  $\approx$  50% was verified by <sup>1</sup>H NMR spectroscopy, using the relative integrations of methylene signals in  $\alpha$ -position of the amid function ( $\delta$  = 2.15 ppm; CH<sub>2</sub>-CONH) and the carboxylic acid function ( $\delta$ =2.30 ppm; CH<sub>2</sub>-COOH, Figure 24). Furthermore, the absence of diagnostic signals of the CH<sub>2</sub>-NH<sub>2</sub> (attributed to the unreacted UDETA at  $\delta$ =2.70 ppm) confirms complete conversion of monomer.

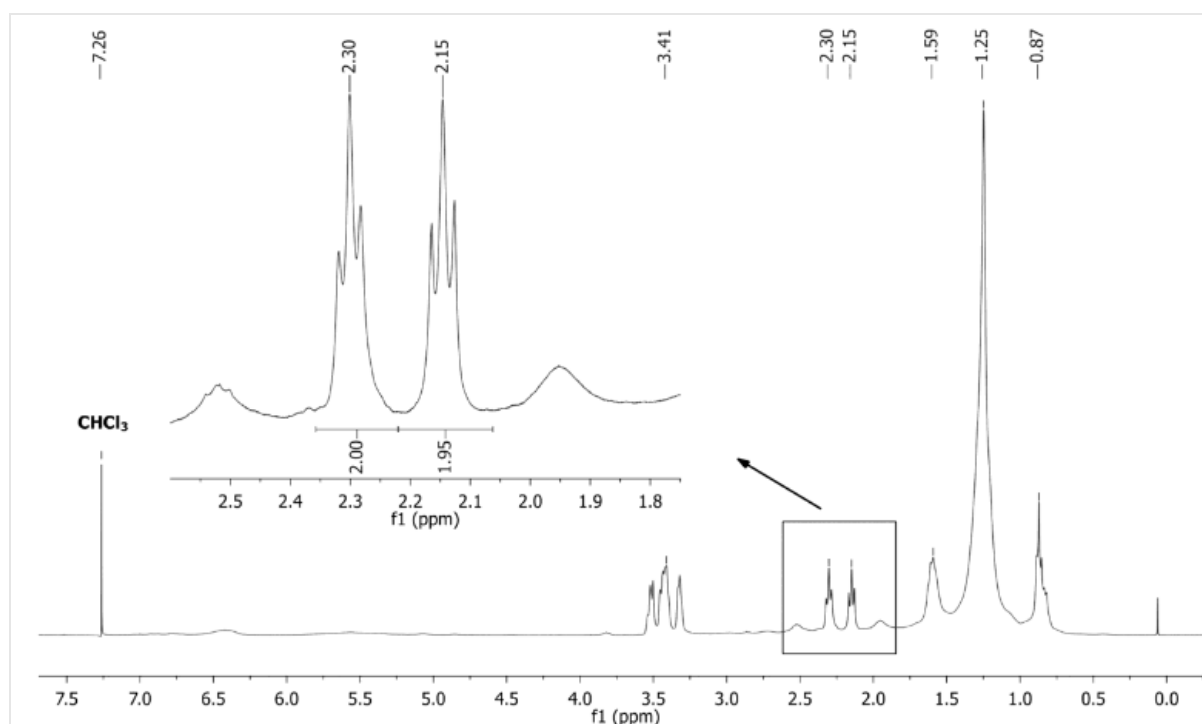


**Figure 24** <sup>1</sup>H NMR spectrum (CDCl<sub>3</sub>, 400 MHz) of SP50 sample. The final conversion of carboxylic acids into amides of around 50% (here 49.4%) was verified using the integration of CH<sub>2</sub>-CONH and CH<sub>2</sub>-COOH signals at 2.15 and 2.30 ppm, respectively.

#### 3.3.1.d. Monitoring of the curing process

Vitrimer hybrid networks were obtained by reacting SP50 with different mixtures of epoxides. Five compositions were investigated by varying the initial ratio [DGEBA]<sub>0</sub>/[TGMDA]<sub>0</sub> from 100/0 to 0/100 (Table 3 ). Data collection and spectroscopic analysis are developed below.

**Table 3 Stoichiometries used for the synthesis of hybrid vitrimer networks with different compositions.**

Sample	[DGEBA] <sub>0</sub> /[TGMDA] <sub>0</sub>	SP50 (g)	DGEBA (g)	TGMDA (g)	Conversion <sup>a)</sup>
1	100 - 0	2.13	0.514	-	100
2	75-25	20.67	3.73	0.81	100
3	50-50	20.8	2.54	1.57	100
4	25-75	19.36	1.16	2.17	94
5	0-100	20.8	-	3.11	83

a) conversion of epoxy functions was evaluated by measuring the intensity of IR epoxy signals in the 920–900 cm<sup>-1</sup> range.

The addition reaction of the carboxylic acid on the epoxide ring has been recently investigated [66]. A model reaction between sebacic acid (bifunctional carboxylic acid) and DGEBA catalyzed by 2-phenylimidazole (2-PI) is fully described for the IR analysis of such network. Attenuated total reflection infrared spectroscopy (ATR-FTIR) was performed using a Specac high-temperature Golden Gate ATR cell mounted on a Bruker Tensor 37 IR spectrometer. Curing took place at 125 °C and the IR data were collected during the first 60 minutes of the process, showing the change in the mixture composition. For this study, most relevant information was found in the 900-2000 cm<sup>-1</sup> wavenumber range shown in Figure 25. Due to the overlapping of signals, monitoring was performed through the integration of absorbance over well-defined intervals. The method of analysis for ATR-FTIR curing and integration of relevant IR signatures can be found below.

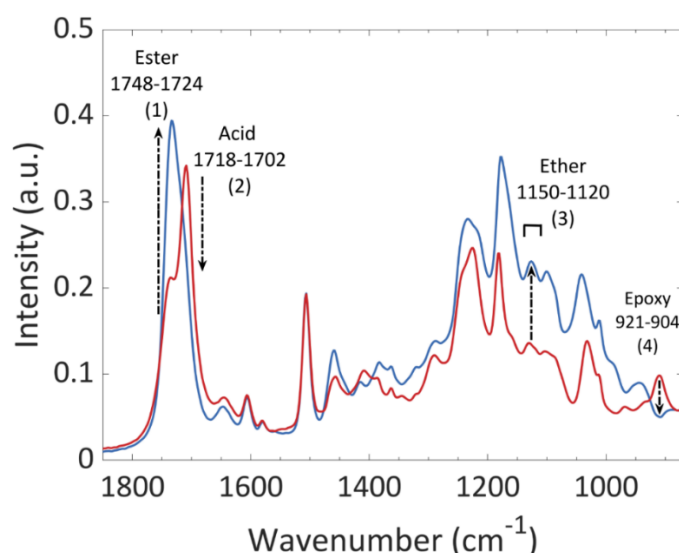


**Figure 25 ATR-FTIR spectral curves of typical epoxy acid reaction at the beginning (red curve) and at the end of the reaction (blue curve). The labelled peaks correspond to: (1) C=O stretching of ester related to the polymer network, (2) C=O stretching of the acid reactant, (3) C-O-C signature of the ether, (4) asymmetric epoxy deformation. The signal integration intervals are indicated, see below for details [66].**

### Data collection

Data were collected using a Bruker Tensor 37 spectrometer equipped with a Specac GoldenGate thermalized ATR stage. Components of reactive mixtures were weighed and mixed together at room temperature in a mortar before placing a drop of the mixture on the golden gate cell preheated to 125 °C. Spectra were then recorded at regular 2 min intervals (resp. 1 min intervals with 2-PI). CO<sub>2</sub>/water vapour correction and noise reduction were applied through the Opus software. Data were then analysed using integration tools in the Opus 3D module.

Figure 26 shows a typical collection of spectra, obtained in the 2000-600 cm<sup>-1</sup> range. Identification of signals in the 1600-1800 cm<sup>-1</sup> range is shown in Figure 27.

### Carbonyl peaks assignment

In Figure 26, major changes are observed in the 1600-1800 cm<sup>-1</sup> region during curing. The signal detected at 1706 cm<sup>-1</sup> is attributed to the C=O stretching of H-bonded dimerized carboxylic acid groups [67]. Another signal, detected at 1735 cm<sup>-1</sup> is attributable to the C=O stretching of the ester. However, for all investigated formulations, a signal at 1735 cm<sup>-1</sup> was already observed before starting the cure cycle while no ester was yet present.

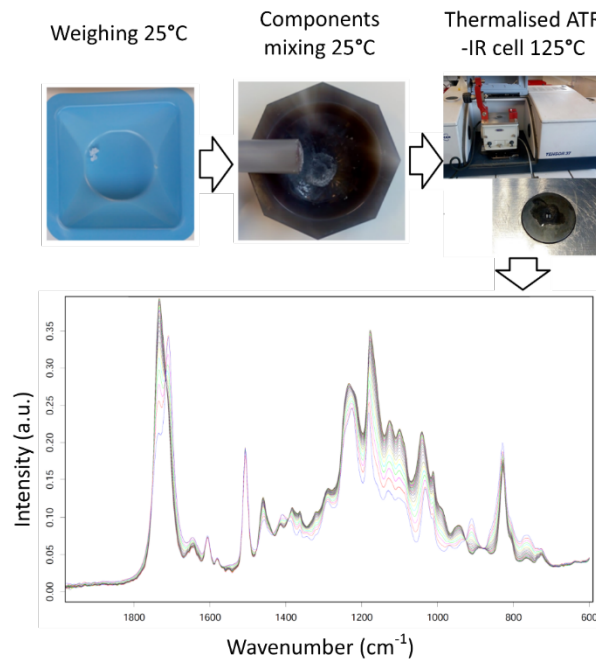


**Figure 26 Schematic of ATR-FTIR curing experiment to record species evolution over time.**

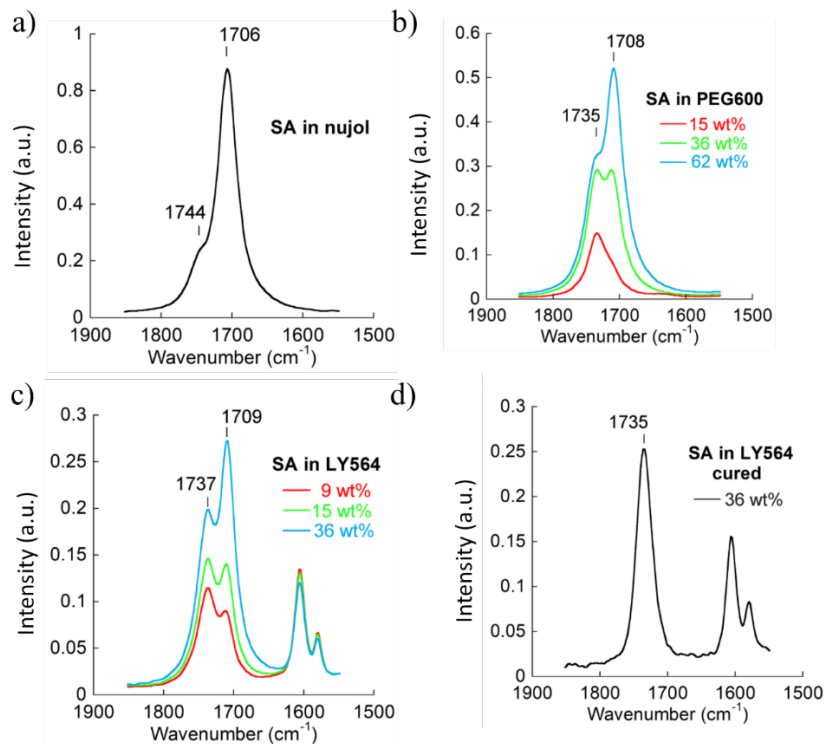


**Figure 27 Identification of C=O stretching signals. a) Sebacic acid in the molten state at 145 °C in paraffin oil. The signal at 1706 cm<sup>-1</sup> is the regular signal of dimerized H-bonded COOH groups, b) Sebacic acid at different concentrations in PEG600 used as a solvent. The signal at 1735 cm<sup>-1</sup> is due to COOH groups interacting through H-bonds with the ether groups of the solvent. c) Sebacic acid at different concentrations in epoxy resin before curing; the same signals as in b) are present. The ether groups of uncured epoxy resin interact with dissolved COOH groups. d) Sebacic acid in epoxy resin after full curing. The signal detected at 1735 cm<sup>-1</sup> may be attributed to the C=O stretching of the ester group.**

Spectra of sebacic acid recorded in various liquid environments and concentrations (Figure 27) lead to the conclusion that the C=O stretching signal of solvated COOH groups (forming a H-bond with surrounding ether groups) overlaps the signal of ester at 1735 cm<sup>-1</sup>.

### Integration of signals

Integration of ATR signals was used for monitoring cure reactions. Integration details are illustrated in Figure 28 for the different functional groups:

- **Esters:** Integration of the C=O stretching peak (1735 cm<sup>-1</sup>) over the 1748–1724 cm<sup>-1</sup> interval.
- **Carboxylic acids:** Integration of the C=O stretching peak (1705 cm<sup>-1</sup>) over the 1718–1703 cm<sup>-1</sup> interval.
- **Epoxides:** Integration of the asymmetric epoxy ring deformation (914 cm<sup>-1</sup>) over the 921–904 cm<sup>-1</sup> interval.
- **Ethers:** Characteristic C-O signals are expected for aliphatic ether functions in the 1140-1100 cm<sup>-1</sup> range . Other C–O stretching signals may interfere with those signals:
  - Aryl-alkyl ether functions: two signals around 1250 cm<sup>-1</sup> and 1040 cm<sup>-1</sup>.
  - Primary and secondary alcohol functions: two signals around 1065 cm<sup>-1</sup> and 1100 cm<sup>-1</sup>.
  - Ester functions: several signals in the 1280-1160 cm<sup>-1</sup> range.

Therefore, to extract a specific signal of ethers formed by the anionic polymerization of the epoxy with minimum interference with other functions present, the ether signature was isolated by integration of the ATR trace between 1150 and 1120  $\text{cm}^{-1}$ , as underlined in red in Figure . Baseline for integration was taken by connecting the maxima of neighbouring peaks at 1182  $\text{cm}^{-1}$  and 1033  $\text{cm}^{-1}$  which showed little change during the reaction.

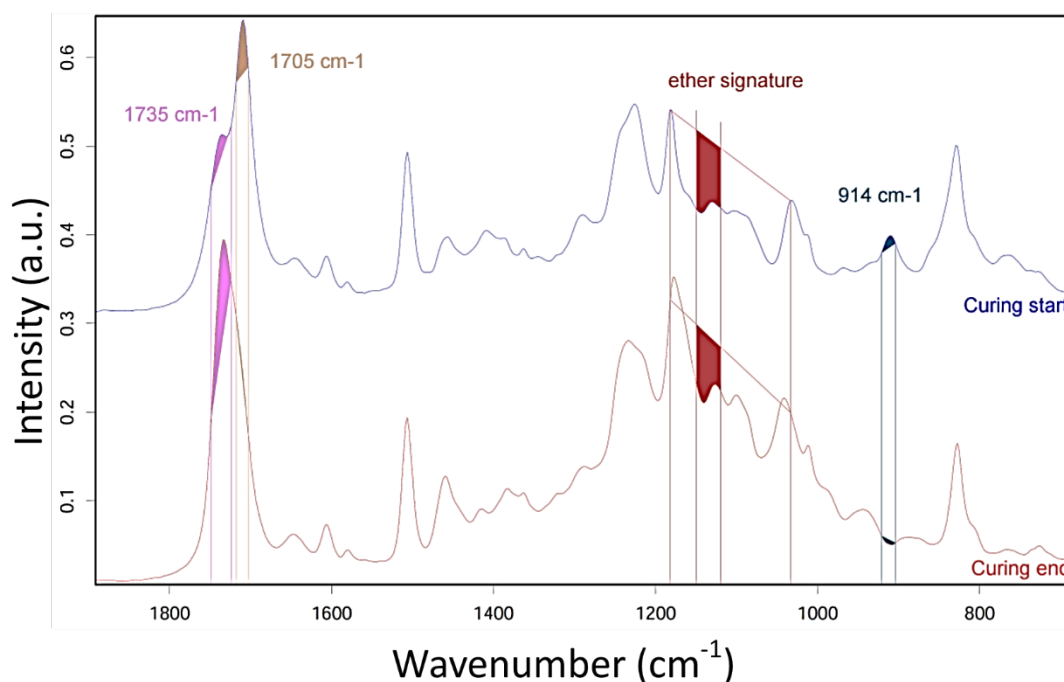


**Figure 28 Typical integration zones at the beginning (blue curve) and at the end (red curve) of cure process for the different functional groups. For epoxy groups, the interval is marked in red.**

### 3.3.1.e. Characterisation of the hybrid vitrimer network

#### Swelling and soluble fraction

**Swelling** studies were performed using samples measuring approximately 5 mm × 5 mm × 3 mm. The samples were weighed and their dimensions measured before immersion in 1,2,4-trichlorobenzene (TCB) at 150 °C, well above the glass transition  $T_g$  of the samples to ensure that swelling equilibrium has been reached. TCB was chosen for its high evaporation temperature (214 °C). Swollen samples were extracted, wiped with a tissue, and stabilized at room temperature for 24 h to avoid any thermal expansion effect; swelling ratio and soluble fraction were calculated by gravimetry for all samples.

**Table 4 Solvent uptake, swelling and gel content values after immersion in trichlorobenzene for 24 h at 150 °C.**

Sample	(DGEBA) <sub>0</sub> /[TGMDA] <sub>0</sub>	Solvent uptake (wt. %)	Swelling (vol. %)	% gel (wt. %)
1	100 - 0	soluble	-	-
2	75-25	354	280	42
3	50-50	221	150	64
4	25-75	184	118	73
5	0-100	158	85	77

#### Thermomechanical characterisation

**Dynamic mechanical analysis (DMA), stress relaxation and creep experiments** were performed using a Q800 DMA (TA Instruments, USA) operating in the film tension geometry on rectangular samples (10 mm × 5 mm × 2 mm) with a heating regime from -50 °C up to 200 °C at 3 °C.min<sup>-1</sup>, and a measurement frequency of 1 Hz following standard procedures to measure the glass transition temperature  $T_g$ . DMA and DSC results are shown in Figure 29. Hybrid networks are referred to as HN-50\_\_\_\_\_.

**Stress relaxation** experiments were conducted in shear mode on rectangular samples (50 mm × 50 mm × 4 mm) applying a 1% strain. The sample is allowed to relax for 500 min at each temperature. Temperature parameters have been adapted for each sample type according to their mechanical properties.

**Creep testing** was performed at room temperature on rectangular samples (10 mm × 5 mm × 2 mm) cut from larger plates to observe bulk relaxation. A film tension geometry system was used and different stresses were applied to the samples: 100, 20, and 2 kPa were used for samples containing 100%, 50%, and 25% of TGMDA, respectively. Creep behaviour of these 3 samples is shown in Figure 30.

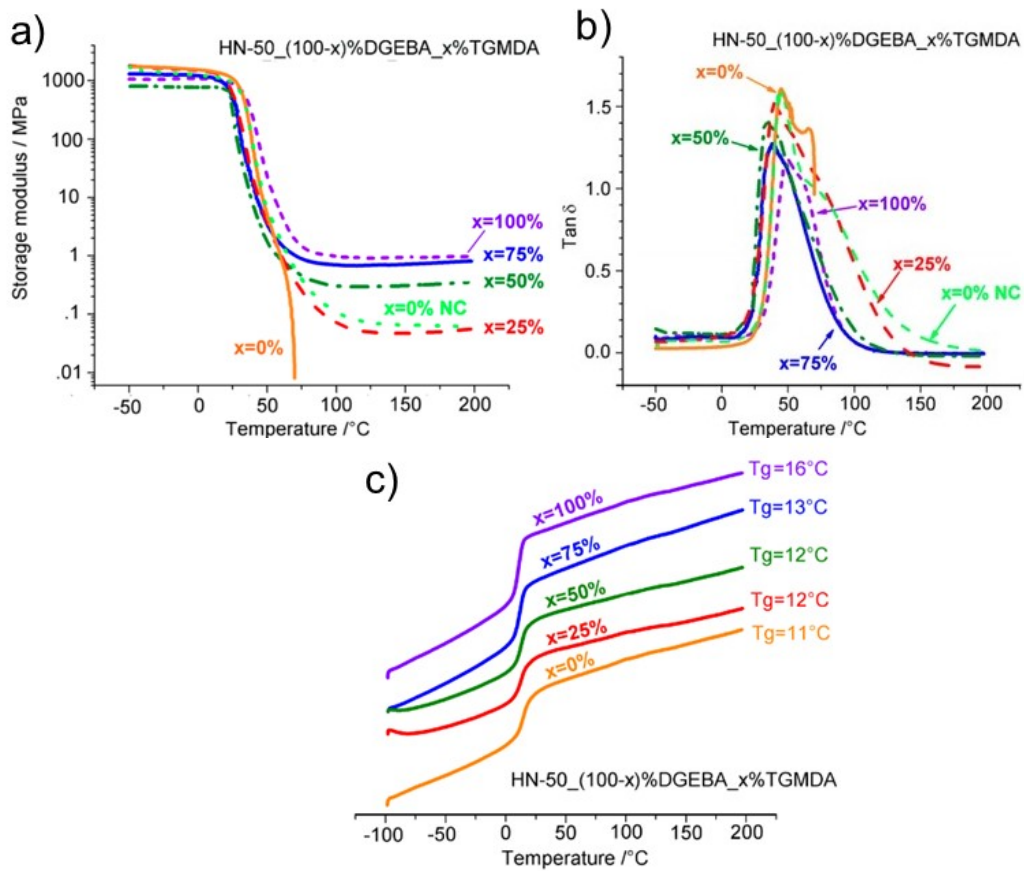


Figure 29 a) Storage modulus, b) Tan  $\delta$  values in a temperature range from -50 °C to 200 °C for hybrid networks HN. c) Estimation of glass transition temperature from DSC measurement.

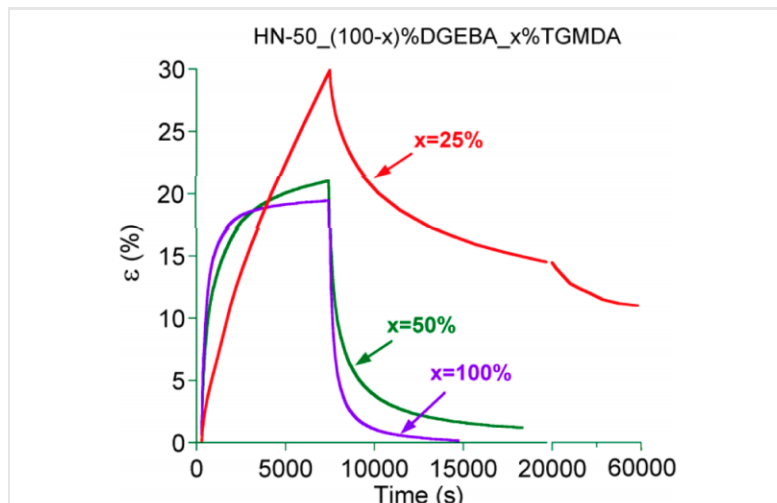


Figure 30 Creep-recovery experiments of compounds HN-50\_0%DGEBA\_100%TGMDA, HN-50\_50%DGEBA\_50%TGMDA, and HN-50\_75%DGEBA\_25%TGMDA for an applied stress of 100, 20, and 2 kPa, respectively.

**Quasi-static tensile tests** were performed at ambient temperature using dog-bone specimens of 6 mm width, 25 mm gauge length, and about 3 mm thickness, based on the ASTM D638-10 normalized shape (sample type IV). The tensile testing machine was used at a constant crosshead displacement rate of 25 mm.min<sup>-1</sup>, and a 1 kN load cell was used to record the load. The deformation was evaluated from the crosshead displacement for the shown data. At least three samples were tested per test condition. The elastic modulus was calculated between 0.05 and 0.25% of the strain at break, the tension energy to break (TEB) was measured as the area below the stress–strain curve.

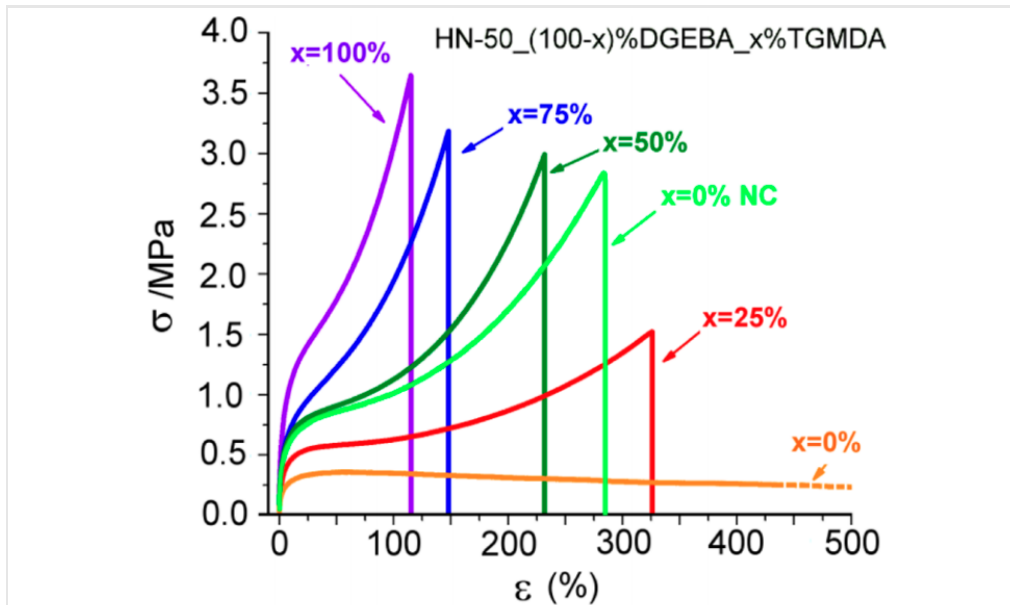


Figure 31 Tensile curves recorded at 22 °C with a deformation rate of 25 mm.min<sup>-1</sup>.

Table 5 Glass transition temperature  $T_g$ , ultimate stress, ultimate strain, elastic modulus measured between 0.05 and 0.25% of deformation, and tensile energy to break (TEB).

Sample	(DGEBA) <sub>0</sub> / [TGMDA] <sub>0</sub>	$T_g$ °C	Ultimate stress MPa	Ultimate strain MPa	Elastic modulus MPa	TEB J.m <sup>-3</sup> ×10 <sup>4</sup>
1	100-0	11	-	> 800	0.2	-
2	75-25	12	1.6	330	0.3	276
3	50-50	12	3.1	230	0.5	344
4	25-75	13	3.2	150	0.6	255
5	0-100	16	3.7	115	0.9	236

The **self-healing efficiency** was measured after cutting dog-bone samples in the middle of the gauge length. Surfaces were then brought in contact by hand pressure and the sample was set in a hard silicon mould for good alignment. The samples were allowed to heal between 1 h and 24 h at constant temperature and subsequently tested on the tensile machine.

The healing efficiency  $\eta$  was calculated from the formula:

$$\eta [\%] = \frac{TEB_{healed}}{TEB_{pristine}} \cdot 100$$

where  $TEB_{healed}$  and  $TEB_{pristine}$  correspond to the tension energy to break of the healed and pristine material, respectively. Result are shown in Figure 32 and Table 6.

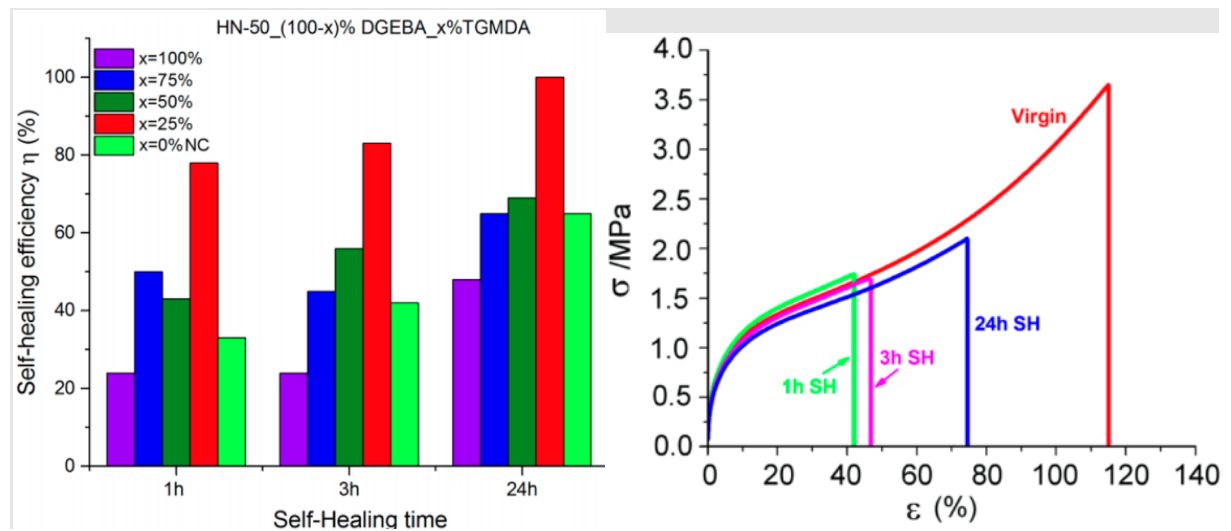


Figure 32 Tensile curves of HN-50\_0%DGEBA\_100%TGMDA (left) and, the self-healing efficiencies  $\eta$  for increasing healing times (1, 3, and 24 h) (right).

Table 6 Self-healing efficiencies  $\eta$  of the hybrid vitrimer networks for increasing self-healing time (1,3 and 24 hours).

Sa mp ple	[DGEBA] <sub>0</sub> /[TGMDA] <sub>0</sub> Compos ition [DGEBA] <sub>0</sub> /[TGMDA] <sub>0</sub>	$\eta$ % 1 h SH	$\eta$ % 3 h SH	$\eta$ % 24 h SH
1	100-0	33	42	65
2	75-25	78	83	complete recovery
3	50-50	43	56	69
4	25-75	50	45	65
5	0-100	24	24	48

### 3.3.2. Electrically conductive materials

The self-healing hybrid networks with graphite reported in deliverable D1.1 were characterized as follows: rectangular samples (dimensions roughly 5 mm x 1 mm x 1 mm) were connected with metal wires and conductive glue at the lateral ends. Voltage (200 V) was applied, the current was measured with a sensitive current meter and therewith the conductivity was calculated. Due to the low conductivity, this preliminary study was discontinued and the integration of other conductive fillers (see sections of conductive fillers of EMPA and VUB) in self-healing networks will be done in future experiments.

**Table 7** Resistance and conductivity of conductive hybrid networks with different amounts of graphite.

Graphite vol%	10	20	30
Resistance $\Omega$	$10^9$	$10^8$	$10^5$
Conductivity $\Omega^{-1} \text{ cm}^{-1}$	$10^{-8}$	$10^{-7}$	$10^{-5}$



**Figure 33** Photograph of graphite-hybrid vitrimer composites from 10 vol.% (left) to 30 vol.% (right) graphite in the hybrid network matrices.

In conclusion, Section 3.3 described the different characterization methods implemented when dealing with hybrid vitrimer networks for soft robotic applications. The “tunability” of such networks, by modifying the amount of hydrogen bond moieties or the crosslinker ratio di/tetra-epoxides, allows the preparation of materials with modifiable thermo-mechanical properties and self-healing capabilities. Key parameters such as cyclic measurements (up to 50% strain) or self-healing ability when the material is subjected to fatigue, damage by overloading or by interfacial debonding are currently under investigation. As the both the chemical compositions and the properties of these materials vary strongly, the characterization protocols need to be continuously updated.

### 3.4. Conductive thermoplastic elastomers (Empa)

In an attempt to show how the characterization for piezoresistive elastomer-based strain sensors can be applied, an anthology of examples is presented.

#### 3.4.1 Tensile test up to the point of fracture: The effect of the loading rate

The first example is from the tensile test up to the point of fracture for two elastomer-based sensor fibers. Both fibers are based on carbon black but two different thermoplastic elastomers are used as matrix materials: a thermoplastic styrene-based elastomer (TPS) and thermoplastic polyurethane (TPU).

The results are part of the study: Georgopoulou Antonia, Sebastian Tutu, & Clemens Frank. (2020). Thermoplastic elastomer composite filaments for strain sensing applications extruded with a fused deposition modelling 3D printer [68].

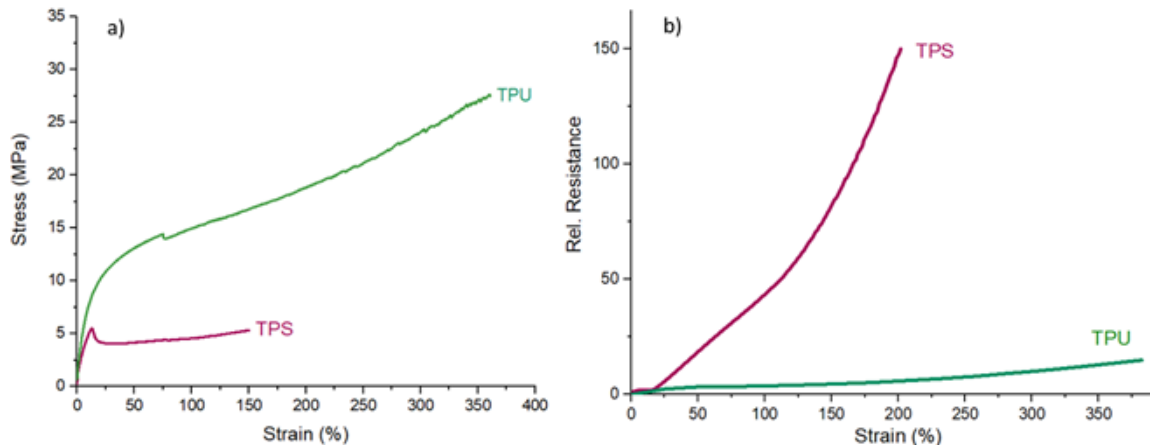


**Figure 34** The a) stress-strain response and b) resistance-strain response for piezoresistive strain sensor fibers based on TPU and TPS. The loading rate was 200 mm/min. Graphs made from data found in [69].

**Table 8** Mechanical properties for the three conductive filaments at different strain rates derived from the tensile test up to the point of fracture. Data found in [69].

Filament	Strain Rate (mm/min)	Stress at yield point (MPa)	Strain at yield point (%)	Stress at point of fracture (MPa)	Strain at point of fracture (%)	Young's modulus (MPa)
TPS	50	5.2	13	4.1	150	35
TPU	50	4.6	12	18.9	493	33
TPS	100	4.2	10	9.5	161	35
TPU	100	4.6	13	20.4	494	34
TPS	200	5.5	13	5.3	150	98
TPU	200	9.4	15	27.5	360	144

From the results, it was seen that the strain rate did not have a significant effect on the stress and strain value at the yield point. The fiber based on the TPU was significantly stiffer than the fiber based on the TPS, a fact that is derived by the value of the stress at the point of fracture. The TPS-based fiber was also the more brittle fiber with a smaller elongation at the point of fracture. As for the Young's modulus, the value was similar for the two fiber sensors especially at low strain rates. At small strain rates, the value of the Young's modulus was not affected by the increase of the strain but that was not the case at high strain rates.

Looking at the response of the sensor signal during the tensile test up to the point of fracture, it was seen that the TPS based sensor showed a more sensitive response than the TPU-based fiber. The TPU-based fiber has a larger functional range, a fact that can be explained by the lower concentration of carbon black (18% w/w). For the TPS-based fiber, the carbon black concentration was 50% w/w. As for the effect of the strain rate, it was seen that increasing the strain rate resulted in higher sensitivity. However, in the case of the TPU, increasing the loading rate to 200 mm/min, affected the linearity of the curve, since the curve could be divided in more linear parts compared to lower strain rates.

**Table 9 The Gauge Factor for the TPS and TPU based fibers, calculated from the tensile test up to the point of fracture. The GF factor was calculated at each linear part of the curve. Data derived from [69].**

Filament	50 mm/min		100 mm/min		200 mm/min	
TPS	GF=21	$\epsilon=0-80\%$	GF=1	$\epsilon=0-74\%$	GF=46	$\epsilon=0-124\%$
	GF=4	$\epsilon=81-130\%$	GF=14	$\epsilon=75-161\%$	GF=115	$\epsilon=124-161\%$
	GF=31	$\epsilon=131-149\%$				
TPU	GF=1	$\epsilon=0-234\%$	GF=5	$\epsilon=0-494\%$	GF=1	$\epsilon=0-140\%$
	GF=0.003	$\epsilon=235-422\%$			GF=3	$\epsilon=141-210\%$
					GF=4	$\epsilon=211-251\%$
					GF=7	$\epsilon=252-361\%$

**3.4.2 Tensile test up to the point of fracture: Analysing a relative resistance-strain plot**

The next example involves piezoresistive strain sensors from the composition TPS with carbon black presented in example 3.4.1. The sensor in this case is integrated in two different substrates of shore hardness 82A and 95A. The method used for the integration was extrusion based additive manufacturing. In some cases, the sensor response during the tensile test up to the point of fracture shows more than one linear regions. The purpose of this example is to show the different regions in the plot relative resistance-strain.

This example is part of the study: Georgopoulou, A., Vanderborcht, B., & Clemens, F. (2021). Multi-material 3D printing of thermoplastic elastomers for development of soft robotic structures with integrated sensor elements. [70]

From the stress-strain response (Figure 35a) it was seen that the sensor integrated in the stiffer substrate (95A) had a smaller elongation at the point of fracture compared to the sensor integrated in the softer substrate. From the response of the sensor, during the tensile testing up to the point of fracture, four areas with the same linearity were found. In both cases, the resistance first increased (I), then decreased (II), then increased again (III) and then in increased with a different slope (IV). Only at high strains (regions III and IV), the sensor showed a positive piezoresistive response.

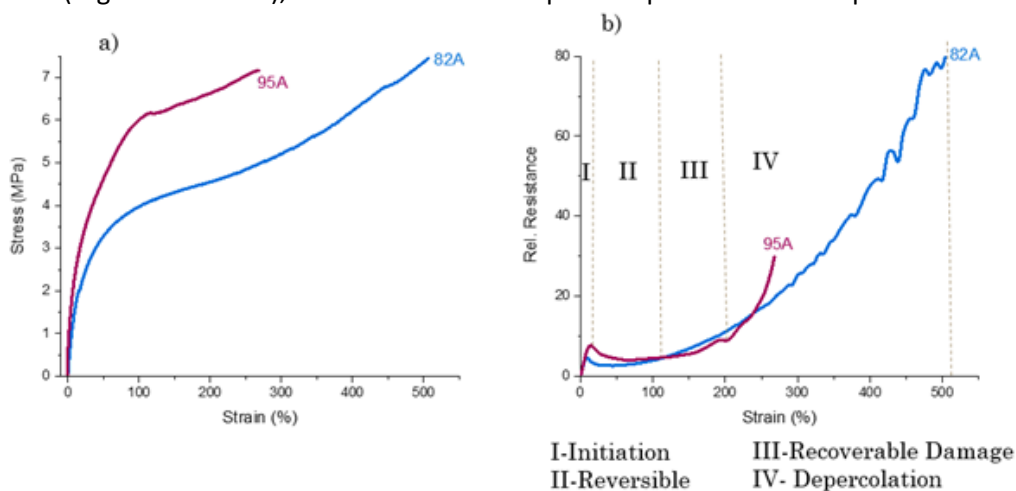


**Figure 35: a) Mechanical and b) Electrical response during the tensile test up to the point of fracture for a piezoresistive strain sensor, integrated in two different shore hardness substrates 95A (purple) and 82A (blue).**

### 3.4.3 Dynamic testing: Linear and non-linear response

The next example is from the same study as in section 3.4.1 [68]. Again two different piezoresistive fibers based on TPS and TPU are being presented. The tensile test in this case, is a dynamic tensile test that involves cyclic straining and releasing.

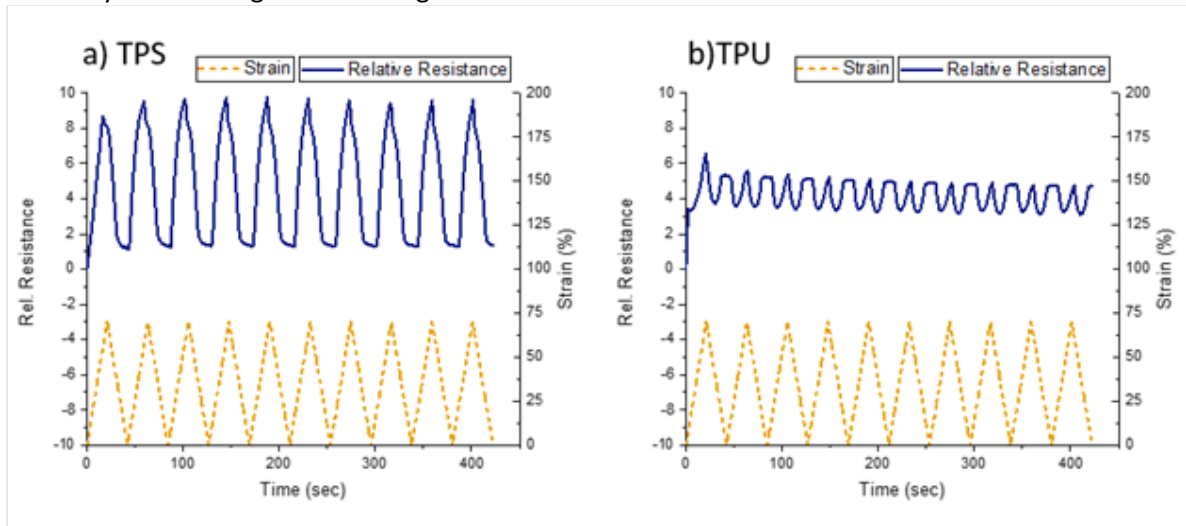


**Figure 36: Dynamic tensile testing for piezoresistive fibers of diameter 0.5m based on a matrix a) TPS and b) TPU. The test involved ten cycles of straining and . between 0-70% strain. The plots were made from data found in [69].**

**Table 10 | Drift, Hysteresis and Uncertainty calculated from the dynamic tensile test for the TPS and TPU based piezoresistive strain sensor data. The data can be found in [69].**

FDM extruded filament	Drift between 2 and 10 cycle		Drift between 9 and 10 cycle		Hysteresis	Uncertainty
	@ 0% strain	@ 70% strain	@ 0% strain	@ 70% strain		
TPS	1.5%	1%	1.5%	0.4%	47%	< 26% strain
TPU	10%	16%	0.6%	0.2%	23%	< 45% strain

\* Because of the behavior of the Eel filaments during the dynamic test.

Looking at the response of the sensor signal, for the two fibers, during the tensile testing, it can be seen that the drift was significantly larger in the case of the TPU based sensor compared to the TPS sensor. On the other hand, the TPS sensor exhibits larger hysteresis compared to the TPU sensor. As for the linearity of the two sensors, there is uncertainty observed for both the sensor fibers. In the case of the TPS-based fiber, the uncertainty appears with the form of a plateau at strain 26% in the releasing part of the cycle. For the TPU-based sensor, the uncertainty appears in the form of a secondary peak. The uncertainty in this case is significantly higher (45%) and is more than half of the range of strain applied in his test. Even though the TPU-based sensor fiber had the smaller hysteresis, the large uncertainty make it an unsuitable option for many applications.

### 3.4.4 Dynamic testing: Defining the uncertainty

The next example explores different ways uncertainty might appear during a dynamic tensile test. The results are part of a study that involved fiber composites with different matrix materials. The sensor

fiber was embedded in matrix of Polydimethylsiloxane (PDMS), Natural Rubber (NR), Pre-vulcanized Natural Rubber (PVNR) and a spring structure integrated in the NR. The full study can be found in [42]. Defining the uncertainty can be a complex task. As it was discussed in the previous section, the uncertainty appears when there is a deviation from linear response. For an ideal strain sensor, the electrical signal should follow the change in strain. The following example shows the response of a sensor fiber, when embedded in different elastomeric matrix materials. The resulting fiber composites were examined with dynamic tensile testing for their performance.

Even for the single fiber, it was seen that there was some uncertainty at low strains in the unloading caused by the appearance of a plateau. This behavior is linked with the presence of buckling during the testing because of creep of the elastomer matrix. When the fiber was embedded in the PVNR (pre-vulcanized natural rubber), the resulting composite had an optimal response. The sensor signal followed the change in strain with high accuracy. For both the NR (natural rubber) and NR+spring fiber composites, there was observed a plateau similar to the one present in the case of the single fiber. For the PDMS fiber composites, instead of a plateau there was the appearance of a secondary peak that caused the uncertainty. From all the cases, because of the effect of the uncertainty, only the PVNR composite could be used for applications that require high precision, even at very low strains.

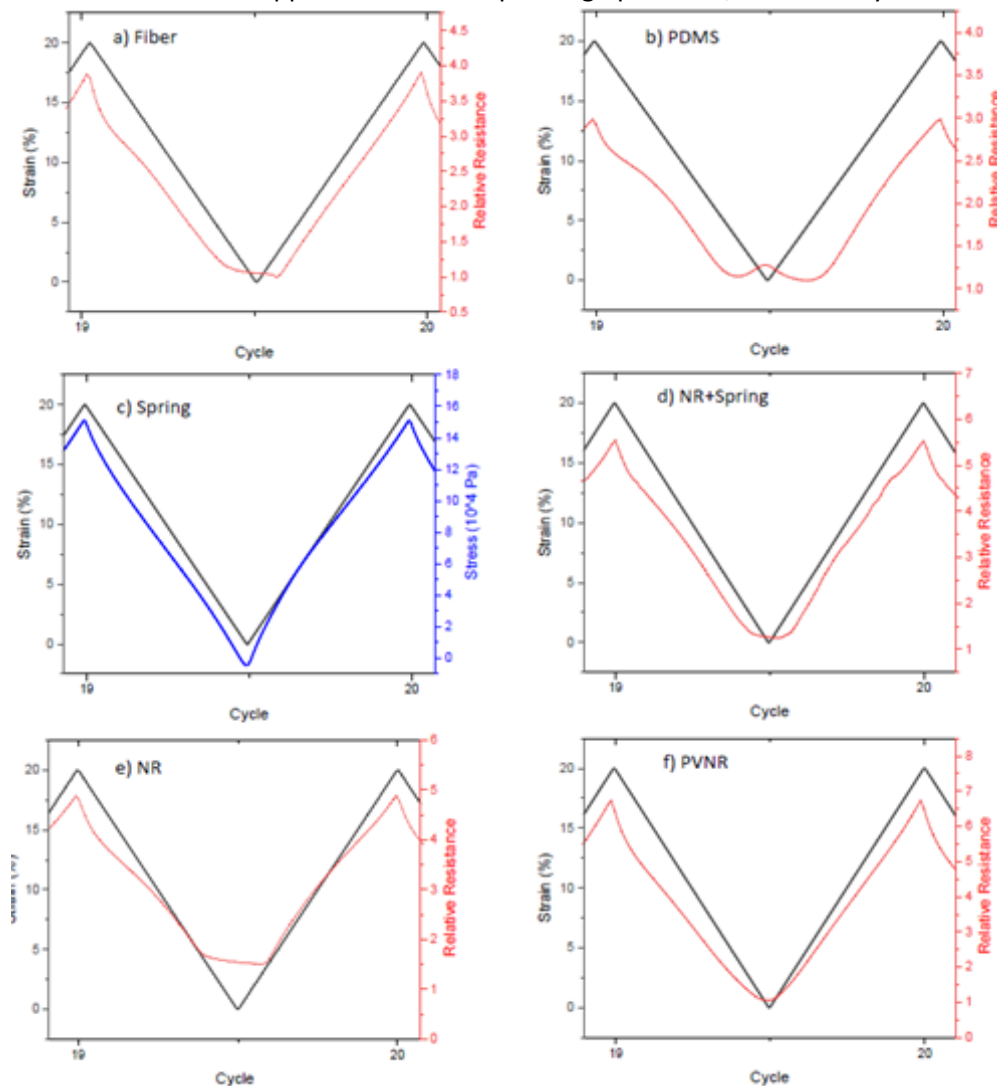


**Figure 37** Overview of the electrical resistance (a,b, d-f) for the fiber sensor composites and the mechanical response of the 3d printed spring structure (c) between the 19th and 20th cycle of the cyclic tensile test. Reproduced under the terms of a cc-by license from [42].

### 3.4.5 Dynamic testing: Hysteresis

In the same study, the hysteresis was calculated for the different fiber composites. For that reason, the relative resistance was plotted with the strain.

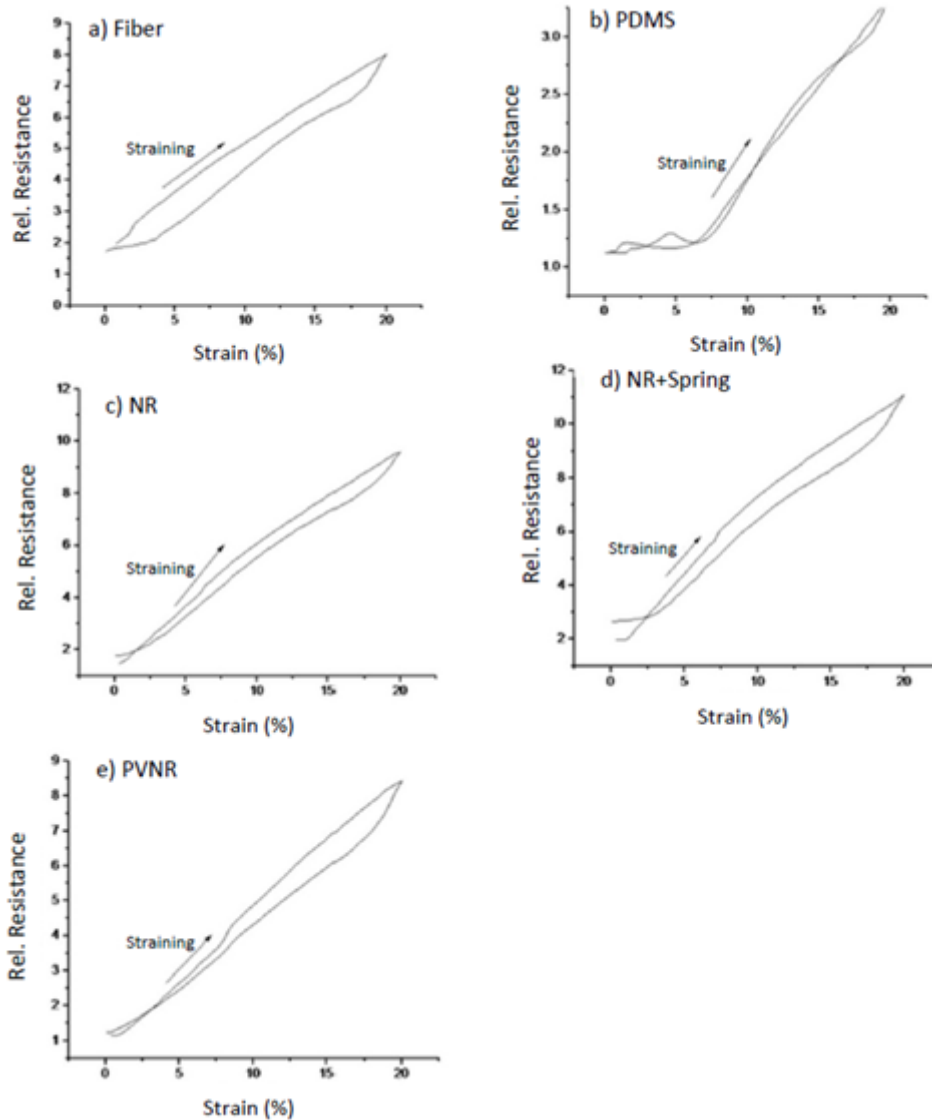


**Figure 38: The relative resistance as a function of the strain during the first cycle of the dynamic testing for a) the single fiber and the fiber embedded in b) PDMS c) Natural Rubber d) Natural Rubber with the spring structure and d) pre-vulcanized natural rubber. Reproduced under the terms of a CC-BY license from [42].**

The hysteresis was calculated at 10 % strain and the values are summarized in the following table.

**Table 11** Hysteresis at 10% strain for different fiber composites. Data derived from [71].

Sensor	Hysteresis at 10% strain (%)
Pure Fiber	15.5
Fiber in PDMS	1.2
Fiber in NR	1.4
Fiber in NR with Spring structure	2.3
Fiber in PVNR	16

As can be seen from Table 11, with the exception of the PVNR, embedding the fiber in the matrix resulted in reducing the hysteresis. The fiber composite with the smaller stiffness (PDMS) exhibited the smaller amount of hysteresis. Including the spring in the NR fiber composite resulted in an increase in the hysteresis.

### 3.4.6 Quasi-static testing : Mechanical and Electrical Relaxation

The first example, shows the fibers introduced in example 3.4.1 and 3.4.3.

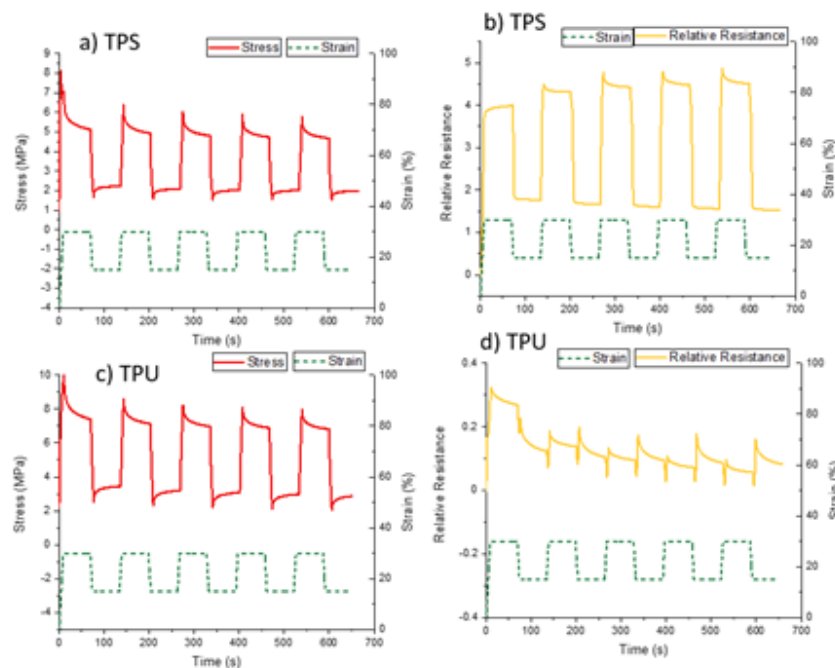


**Figure 39: Mechanical and electrical relaxation for piezoresistive sensor fibers based on TPS and TPU. Data derived from [69].**

The response shows the presence of mechanical relaxation for both the TPS and the TPU. The mechanical relaxation was larger in the case of TPS. However, because of the bad linearity of the TPU based sensor it was not possible to distinguish based on the value of the relative resistance, if the sensor was at strain 15% or 35%.

As for the mechanical relaxation, in the case of the TPS based sensor fiber, the value does not change significantly at high and low strains. This is not the case for the TPU-based fiber, where the amount of relaxation at low strains is double the percentage of relaxation at high strains. As for the electrical

relaxation, the value is significantly higher for the TPU based fiber, compared to the TPS fiber at high and low strains.

**Table 12 Mechanical and Electrical Relaxation of the monofilament fibers calculated at the third cycle of the dynamic testing dwell time. The relaxation was calculated at high (35%) and low (15%) strains.**

Filament	Mechanical Relaxation (%)		Electrical Relaxation (%)	
	High Strains	Low Strains	High Strains	Low Strains
TPS	23	29	12	8
TPU	17	36	63	40

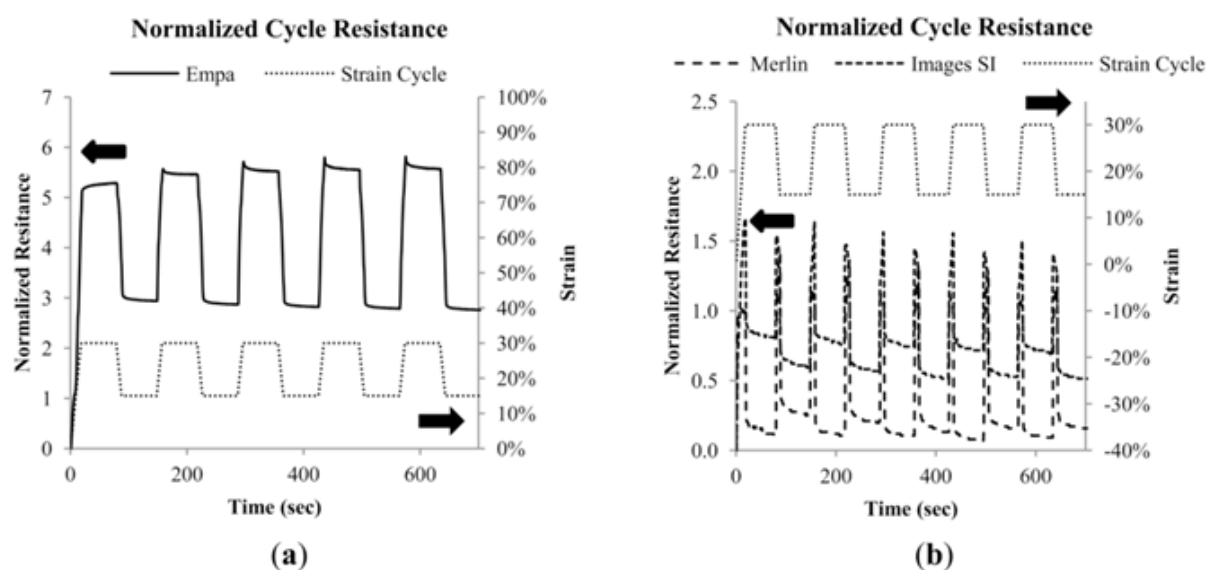


**Figure 40: Cyclic (15%–30%) tensile loading behavior of the Empa 0.3 mm monofilaments and (b) behavior of the Images SI, and Merlin monofilaments, with strain cycle included for reference. Reproduced under the terms of a CC BY license from [72].**

In this example, the selected materials show different behavior when it comes to detecting the strain during the dwell time. This example comes from a study of comparing different piezoresistive sensor fibers. In figure 40a, the response of the Empa fiber can be seen. The empa fiber consists of a TPS elastomer and carbon black in concentration 50% w/w. In this case, it can be seen that the electrical signal follows the change in strain and even if there is electrical relaxation present, it is possible to distinguish when strain 15% or 30% is exerted on the fiber. This response was compared to commercial piezoresistive sensor fibers (Figure 40b). In this case, it was seen that the signal does not follow the change in strain. Especially during the dwell time, the signal dropped significantly and it was not possible to distinguish the strain based on the value of the signal during the dwell time.

## 4. References

- [1] <http://www.softroboticsinc.com/>, (n.d.).
- [2] <http://www.empirerobotics.com/>, (n.d.).
- [3] <https://onrobot.com/en>, (n.d.).
- [4] <https://www.piab.com/Products/advanced-gripping-solutions/>, (n.d.).
- [5] <http://en.softrobottech.com/>, (n.d.).
- [6] <https://www.softroboticgripper.com/>, (n.d.).
- [7] J. Shintake, V. Cacucciolo, D. Floreano, H. Shea, Soft Robotic Grippers, *Advanced Materials*. 30 (2018) 1707035. doi:10.1002/adma.201707035.
- [8] C. Piazza, G. Grioli, M.G. Catalano, A. Bicchi, A Century of Robotic Hands, *Annual Review of Control, Robotics, and Autonomous Systems*. 2 (2019) 1–32. doi:10.1146/annurev-control-060117-105003.
- [9] J. Amend, N. Cheng, S. Fakhouri, B. Culley, Soft robotics commercialization: jamming grippers from research to product, *Soft Robotics*. 3 (2016) 213–222. doi:10.1089/soro.2016.0021.
- [10] G. Miron, B. Bédard, J.S. Plante, Sleeved bending actuators for soft grippers: A durable solution for high force-to-weight applications, *High-Throughput*. 7 (2018). doi:10.3390/act7030040.
- [11] Z. Wang, M. Zhu, S. Kawamura, S. Hirai, Comparison of different soft grippers for lunch box packaging, *Robotics and Biomimetics*. 4 (2017) 1–9. doi:10.1186/s40638-017-0067-1.
- [12] J. Lessing, R. Knopf, K. Alcedo, C. Springs, D. Harburg, S.P. Singh, Soft robotic grippers for cluttered grasping environments, high acceleration movements, food manipulation, and automated storage and retrieval systems, 2017.
- [13] Z. Wang, Y. Torigoe, S. Hirai, A Prestressed Soft Gripper: Design, Modeling, Fabrication, and Tests for Food Handling, *IEEE Robotics and Automation Letters*. 2 (2017) 1909–1916. doi:10.1109/LRA.2017.2714141.
- [14] N. Cheng, J. Amend, T. Farrell, D. Latour, C. Martinez, J. Johansson, A. McNicoll, M. Wartenberg, S. Naseef, W. Hanson, W. Culley, Prosthetic Jamming Terminal Device: A Case Study of Untethered Soft Robotics, *Soft Robotics*. 3 (2016) 205–212. doi:10.1089/soro.2016.0017.
- [15] J. Saldien, K. Goris, B. Vanderborcht, J. Vanderfaillie, D. Lefeber, Expressing emotions with the social robot probot, *International Journal of Social Robotics*. 2 (2010) 377–389. doi:10.1007/s12369-010-0067-6.
- [16] M. Runciman, A. Darzi, G.P. Mylonas, Soft Robotics in Minimally Invasive Surgery, *Soft Robotics*. 6 (2019) 423–443. doi:10.1089/soro.2018.0136.
- [17] H. Liu, M. Selvaggio, P. Ferrentino, R. Moccia, S. Pirozzi, U. Bracale, F. Ficuciello, The MUSHA Hand II : A Multi-Functional Soft Hand for Robot-Assisted Laparoscopic Surgery, *IEEE/ASME Transactions on Mechatronics*. (2020).
- [18] S. Li, H. Bai, R.F. Shepherd, H. Zhao, Bio-inspired Design and Additive Manufacturing of Soft Materials, *Machines, Robots, and Haptic Interfaces, Angewandte Chemie - International Edition*. 58 (2019) 11182–11204. doi:10.1002/anie.201813402.
- [19] H. Rodrigue, W. Wang, M.W. Han, T.J.Y. Kim, S.H. Ahn, An Overview of Shape Memory Alloy-Coupled Actuators and Robots, *Soft Robotics*. 4 (2017) 3–15.

- doi:10.1089/soro.2016.0008.
- [20] J. Leng, X. Lan, Y. Liu, S. Du, Shape-memory polymers and their composites: Stimulus methods and applications, *Progress in Materials Science*. 56 (2011) 1077–1135. doi:10.1016/j.pmatsci.2011.03.001.
- [21] J. Shang, X. Le, J. Zhang, T. Chen, P. Theato, Trends in polymeric shape memory hydrogels and hydrogel actuators, *Polymer Chemistry*. 10 (2019) 1036–1055. doi:10.1039/c8py01286e.
- [22] Walker, Zidek, Harbel, Yoon, Strickland, Kumar, Shin, Soft Robotics: A Review of Recent Developments of Pneumatic Soft Actuators, *Actuators*. 9 (2020) 3. doi:10.3390/act9010003.
- [23] A.D. Marchese, R.K. Katzschnmann, D. Rus, A recipe for soft fluidic elastomer robots, *Soft Robotics*. 2 (2015) 7–25. doi:10.1089/soro.2014.0022.
- [24] M.A. Robertson, J. Paik, New soft robots really suck : Vacuum-powered systems empower diverse capabilities, (2017) 1–12.
- [25] K. Urdl, A. Kandelbauer, W. Kern, U. Müller, M. Thebault, E. Zikulnig-Rusch, Self-healing of densely crosslinked thermoset polymers—a critical review, *Progress in Organic Coatings*. 104 (2017) 232–249. doi:10.1016/j.porgcoat.2016.11.010.
- [26] B. Mosadegh, P. Polygerinos, C. Keplinger, S. Wennstedt, R.F. Shepherd, U. Gupta, J. Shim, K. Bertoldi, C.J. Walsh, G.M. Whitesides, Pneumatic networks for soft robotics that actuate rapidly, *Advanced Functional Materials*. 24 (2014) 2163–2170. doi:10.1002/adfm.201303288.
- [27] P. Polygerinos, Z. Wang, K.C. Galloway, R.J. Wood, C.J. Walsh, Soft robotic glove for combined assistance and at-home rehabilitation, *Robotics and Autonomous Systems*. 73 (2015) 135–143. doi:10.1016/j.robot.2014.08.014.
- [28] S. Terryn, J. Brancart, E. Roels, G. Van Assche, B. Vanderborght, Room temperature self-healing of soft pneumatic robotic actuators, *IEEE Robotics & Automation Magazine (RAM)*. Accepted f (2021).
- [29] G. Van Assche, A. Van Hemelrijck, H. Rahier, B. Van Mele, Modulated differential scanning calorimetry: Non-isothermal cure, vitrification, and devitrification of thermosetting systems, *Thermochimica Acta*. 286 (1996) 209–224. doi:10.1016/0040-6031(96)03005-5.
- [30] G. Van Assche, A. Van Hemelrijck, H. Rahier, B. Van Mele, Modulated differential scanning calorimetry : isothermal cure and vitrification of thermosetting systems, 268 (1995) 121–142.
- [31] S. Swier, G. Van Assche, B. Van Mele, Reaction kinetics modeling and thermal properties of epoxy-amines as measured by modulated-temperature DSC. I. Linear step-growth polymerization of DGEBA + aniline, *Journal of Applied Polymer Science*. 91 (2004) 2798–2813. doi:10.1002/app.13466.
- [32] S. Swier, G. Van Assche, B. Van Mele, Reaction Kinetics Modeling and Thermal Properties of Epoxy–Amines as Measured by Modulated–Temperature DSC. II. Network-Forming DGEBA + MDA, *Journal of Applied Polymer Science*. 91 (2004) 2814–2833. doi:10.1002/app.13466.
- [33] A. Cuvellier, R. Verhelle, J. Brancart, B. Vanderborght, G. Van Assche, H. Rahier, The influence of stereochemistry on the reactivity of the Diels-Alder cycloaddition and the implications for reversible network polymerization, *Polymer Chemistry*. Accepted

- (2019). doi:10.1039/C8PY01216D.
- [34] J. Brancart, J. Van Damme, F. Du Prez, G. Van Assche, Thermal dissociation of anthracene photodimers in the condensed state: kinetic evaluation and complex phase behaviour, *Physical Chemistry Chemical Physics*. 22 (2020) 17306–17313. doi:10.1039/d0cp03165h.
- [35] J. Brancart, R. Verhelle, J. Mangialetto, G. Van Assche, Coupling the microscopic healing behaviour of coatings to the thermoreversible Diels-Alder network formation, *Coatings*. 9 (2019). doi:10.3390/coatings9010013.
- [36] J. Mangialetto, A. Cuvellier, R. Verhelle, J. Brancart, H. Rahier, G. Van Assche, N. Van Den Brande, B. Van Mele, Diffusion- And Mobility-Controlled Self-Healing Polymer Networks with Dynamic Covalent Bonding, *Macromolecules*. 52 (2019) 8440–8452. doi:10.1021/acs.macromol.9b01453.
- [37] D. Ehrhardt, K. Van Durme, J.F.G.A. Jansen, B. Van Mele, N. Van den Brande, Self-healing UV-curable polymer network with reversible Diels-Alder bonds for applications in ambient conditions, *Polymer*. 203 (2020) 122762. doi:10.1016/j.polymer.2020.122762.
- [38] D. Ehrhardt, J. Mangialetto, J. Bertouille, K. Van Durme, B. Van Mele, N. Van den Brande, Self-healing in mobility-restricted conditions maintaining mechanical robustness: Furan–maleimide diels–alder cycloadditions in polymer networks for ambient applications, *Polymers*. 12 (2020) 1–24. doi:10.3390/polym12112543.
- [39] H. Winter, F. Chambon, Analysis of Linear Viscoelasticity of a Crosslinking Polymer at the Gel Point.pdf, *Journal of Rheology*. (1986).
- [40] E. Roels, S. Terry, J. Brancart, R. Verhelle, G. Van Assche, B. Vanderborght, Additive Manufacturing for Self-Healing Soft Robots, *Soft Robotics*. 00 (2020) 1–13. doi:10.1089/soro.2019.0081.
- [41] A. Georgopoulou, F. Clemens, Piezoresistive Elastomer-Based Composite Strain Sensors and Their Applications, *ACS Applied Electronic Materials*. 2 (2020) 1826–1842. doi:10.1021/acsaelm.0c00278.
- [42] A. Georgopoulou, C. Kummerlöwe, F. Clemens, Effect of the elastomer matrix on thermoplastic elastomer-based strain sensor fiber composites, *Sensors (Switzerland)*. 20 (2020) 1–15. doi:10.3390/s20082399.
- [43] J. Brancart, M.M. Diaz Acevedo, G. Van Assche, B. Van Mele, Room-Temperature versus Heating-Mediated Healing of a Diels-Alder Crosslinked Polymer Network, *Polymer*. Submitted (2018).
- [44] G. Scheltjens, J. Brancart, I. Graeve, B. Mele, H. Terry, G. Assche, Self-healing property characterization of reversible thermoset coatings, *Journal of Thermal Analysis and Calorimetry*. 105 (2011) 805–809. doi:10.1007/s10973-011-1381-4.
- [45] G. Scheltjens, M.M. Diaz, J. Brancart, G. Van Assche, B. Van Mele, A self-healing polymer network based on reversible covalent bonding, *Reactive and Functional Polymers*. 73 (2013) 413–420. doi:10.1016/j.reactfunctpolym.2012.06.017.
- [46] M.M. Diaz, G. Van Assche, F.H.J. Maurer, B. Van Mele, Thermophysical characterization of a reversible dynamic polymer network based on kinetics and equilibrium of an amorphous furan-maleimide Diels-Alder cycloaddition, *Polymer*. 120 (2017) 176–188. doi:10.1016/j.polymer.2017.05.058.
- [47] W.H. Stockmayer, Theory of Molecular Size Distribution and Gel Formation in Branched-Chain Polymers, *The Journal of Chemical Physics*. 11 (1943) 45–55.

- doi:10.1063/1.1723803.
- [48] J. Brancart, R. Verhelle, J. Mangialetto, G. Van Assche, Coupling the Microscopic Healing Behaviour of Coatings to the Thermoreversible Diels-Alder Network Formation, *Coatings*. 9 (2018).
- [49] E. Roels, S. Terryn, J. Brancart, G. Van Assche, B. Vanderborght, A multi-material self-healing soft gripper, in: *IEEE International Conference on Soft Robotics (RoboSoft)*, 2019: pp. 316–321. doi:10.1109/ROBOSOFT.2019.8722781.
- [50] S. Terryn, E. Roels, G. Van Assche, B. Vanderborght, Self-Healing and High Interfacial Strength in Multi- Material Soft Pneumatic Robots via Reversible Diels-Alder Bonds, *Actuators: Special Issue on Pneumatic Soft Actuators*. 9 (2020) 1–17. doi:10.3390/act9020034.
- [51] S. Terryn, J. Brancart, E. Roels, G. Van Assche, B. Vanderborght, Room-temperature self-healing in soft pneumatic robotics, *IEEE-RAM: Special Issue on Design Optimization of Soft Robots*. (2020).
- [52] J.P. Pascault, R.J.J. Williams, Relationships between glass transition temperature and conversion, *Polymer Bulletin*. 24 (1990) 115–121. doi:10.1007/BF00298330.
- [53] S. Terryn, J. Brancart, D. Lefeber, G. Van Assche, B. Vanderborght, Self-healing soft pneumatic robots, *Science Robotics*. 2 (2017).
- [54] S. Terryn, G. Mathijssen, J. Brancart, T. Verstraten, G. Van Assche, B. Vanderborght, Toward Self-Healing Actuators: A Preliminary Concept, *IEEE Transactions on Robotics*. 32 (2016) 736–743. doi:10.1109/TRO.2016.2558201.
- [55] J. Diani, B. Fayolle, P. Gilormini, J. Diani, B. Fayolle, P. Gilormini, A review on the Mullins effect To cite this version : HAL Id : hal-00773015, (2013) 601–612.
- [56] A.R. Payne, The dynamic properties of carbon black loaded natural rubber vulcanizates. Part II, *Journal of Applied Polymer Science*. 6 (1962) 368–372. doi:10.1002/app.1962.070062115.
- [57] S. Terryn, G. Mathijssen, J. Brancart, D. Lefeber, G. Van Assche, B. Vanderborght, Development of a self-healing soft pneumatic actuator: a first concept, *Bioinspiration & Biomimetics*. 10 (2015) 046007.
- [58] S. Terryn, J. Brancart, D. Lefeber, G. Van Assche, B. Vanderborght, A pneumatic artificial muscle manufactured out of self-healing polymers that can repair macroscopic damages, *IEEE Robotics and Automation Letters*. 3 (2017) 16–21.
- [59] D. Montarnal, F. Tournilhac, M. Hidalgo, J.L. Couturier, L. Leibler, Versatile one-pot synthesis of supramolecular plastics and self-healing rubbers, *Journal of the American Chemical Society*. 131 (2009) 7966–7967. doi:10.1021/ja903080c.
- [60] P. Cordier, F. Tournilhac, C. Soulié-Ziakovic, L. Leibler, Self-healing and thermoreversible rubber from supramolecular assembly, *Nature*. 451 (2008) 977–80. doi:10.1038/nature06669.
- [61] F. Maes, D. Montarnal, S. Cantournet, F. Tournilhac, L. Corté, L. Leibler, Activation and deactivation of self-healing in supramolecular rubbers, *Soft Matter*. 8 (2012) 1681–1687. doi:10.1039/c2sm06715c.
- [62] R. Agnaou, M. Capelot, S. Tencé-Girault, F. Tournilhac, L. Leibler, Supramolecular thermoplastic with 0.5 Pa·s melt viscosity, *Journal of the American Chemical Society*. 136 (2014) 11268–11271. doi:10.1021/ja505956z.
- [63] M. Capelot, D. Montarnal, L. Leibler, Metal-catalyzed transesterification for healing and

- assembling of thermosets, *Journal of the American Chemical Society*. 134 (2012) 7664–7667.
- [64] Y. Wu, Y. Wei, Y. Ji, Polymer actuators based on covalent adaptable networks, *Polymer Chemistry*. (2020). doi:10.1039/d0py00075b.
- [65] F. Sordo, S.J. Mougner, N. Loureiro, F. Tournilhac, V. Michaud, Design of Self-Healing Supramolecular Rubbers with a Tunable Number of Chemical Cross-Links, *Macromolecules*. 48 (2015) 4394–4402. doi:10.1021/acs.macromol.5b00747.
- [66] V. Rebizant, A.S. Venet, F. Tournilhac, E. Girard-Reydet, C. Navarro, J.P. Pascault, L. Leibler, Chemistry and mechanical properties of epoxy-based thermosets reinforced by reactive and nonreactive SBMX block copolymers, *Macromolecules*. 37 (2004) 8017–8027. doi:10.1021/ma0490754.
- [67] A. Georgopoulou, T. Sebastian, F. Clemens, Thermoplastic elastomer composite filaments for strain sensing applications extruded with an FDM 3D printer, *Flexible and Printed Electronics*. (2020).